communications biology

A Nature Portfolio journal

Article

https://doi.org/10.1038/s42003-026-10194-z

Single-cell transcriptomics highlights macrophage-driven regulation of EndMT and repair in injured muscle

Filipa Timóteo-Ferreira[1], Mauro Bergamaschi[1], Riccardo Gamberale[1], Cristiana Barone[1], Cristina D'Orlando[1], Anna Sofia Tascini[2], Veronica Bonalume[3], Raffaella Meneveri[1], Alessandro Fantin[3], Emanuele Azzoni[1,4,5] & Silvia Brunelli[1,4,5]

Following muscle injury, a series of well-coordinated events ensures proper healing. Among these, inflammatory cells, particularly macrophages (MPs), play a fundamental role by phagocytosing damaged tissue and coordinating the actions of other cells involved in regeneration. Partial depletion of infiltrating MPs has been associated with endothelial cells (ECs) undergoing endothelial-to-mesenchymal transition (EndMT), contributing to extracellular matrix accumulation. However, the specific mechanisms linking MPs to this process, as well as their role in influencing EC fate, remain unclear. Here, we adopt a single-cell transcriptomics approach in mice to define a specific signature of the regenerating muscle niche. We show that perturbing MP recruitment upon injury results in impaired MP polarization, creating an aberrant inflammatory, non-regenerative, and less angiogenic microenvironment, which in turn drives ECs toward EndMT. Furthermore, we highlight complex signalling interactions between MPs and ECs, with SPP1 emerging as one of the critical modulators of these processes.

The regeneration of skeletal muscle relies on a complex network of interactions between tissue-resident and recruited cells that develops across different regenerative stages. Following muscle injury, an inflammatory response is triggered, leading to the recruitment of blood-derived monocytes that differentiate into inflammatory macrophages (MPs) upon arrival at the damaged site[1]. These inflammatory MPs secrete a variety of factors that prompt myogenesis and activate the surrounding muscle populations, collectively known as the regenerating muscle niche[2]. This niche supports and appropriately signals the healing process, being composed, among others, by muscle stem cells (MuSCs), which are the primary cells that differentiate into newly regenerated fibres; fibro-adipogenic progenitors (FAPs), mainly involved in extracellular matrix (ECM) turnover; and endothelial cells (ECs), responsible for tissue revascularization[3].

The success of the repair process depends on a timely and balanced transition from a pro-inflammatory to an anti-inflammatory/regenerative environment. This transition is primarily driven by the polarization of the existing MP population in the muscle. By the end of day 3 post-injury, the previously recruited MPs shift from an inflammatory towards an anti-inflammatory/regenerative phenotype[1,4,5], that is accompanied by a metabolic change from glycolysis to oxidative phosphorylation and glutamine metabolism[5,6]. In the event that this transition is disrupted by experimental or pathological factors, the secretion of cytokines and growth factors becomes imbalanced and the fate of MuSCs, FAPs and ECs is altered, ultimately leading to failed muscle regeneration and often fibrosis[4,7,8]. Although FAPs are considered the main contributors to ECM deposition through their ability to differentiate into collagen-producing fibroblasts and/or adipocytes[3,7,9], recent research has highlighted that ECs can also contribute to fibrosis[8,10,11]. A dysregulated inflammatory muscle environment can trigger endothelial-to-mesenchymal transition (EndMT), a process where ECs lose their endothelial function and phenotype and differentiate into ECM-producing mesenchymal cells[8,10]. Nonetheless, further research is required to fully elucidate the cellular and molecular mechanisms driving EndMT in the muscle, as well as the role of MPs in influencing this process.

In this study, we sought to elucidate the role of MPs in muscle regeneration by performing single-cell transcriptomics on the regenerating skeletal muscle niche. We focused on the crosstalk between MPs and ECs and its influence on ECs behaviour. We found that an impairment in MP recruitment dynamics leads to significant changes in the cellular composition of the regenerating muscle niche, with ECs suffering a transformation

[1]School of Medicine and Surgery, University of Milano-Bicocca, Monza, Italy. [2]Center for Omics Sciences, IRCCS Ospedale San Raffaele, Milano, Italy. [3]Department of Biosciences, University of Milano, Milano, Italy. [4]Fondazione IRCCS San Gerardo dei Tintori, Monza, Italy. [5]These authors contributed equally: Emanuele Azzoni, Silvia Brunelli. e-mail: silvia.brunelli@unimib.it

towards a mesenchymal phenotype that ultimately jeopardizes both angiogenesis and myogenesis. In addition, we uncover SPP1 as a cytokine produced by MPs involved in the crosstalk with ECs and with impact on their phenotypic fate and on the onset of EndMT in vivo.

Results

Single-cell RNA sequencing reveals that impaired macrophage recruitment after injury alters the cellular composition of the muscle regenerating niche

Cdh5-CreER^{T2} transgenic mice expressing a tamoxifen (TAM)-inducible form of Cre recombinase (*CRE-ER^{T2}*) under the control of the endothelial-specific gene VE-Cadherin (*Cdh5*) were crossed with *R26R-tdTomato* homozygous reporter mice. To obtain insight on the crosstalk between innate immune cells and vascular-associated cells in vivo, the transcriptome of the regenerating muscle niche of *Cdh5-CreER^{T2}:R26R-tdTomato* mice was analyzed after partial ablation of infiltrating MPs. To this purpose, Cre recombination was induced in *Cdh5-CreER^{T2}:R26R-tdTomato* mice with three consecutive subcutaneous (SC) injections of tamoxifen (TAM) at postnatal days 6, 7, and 8. Thus, virtually all postnatal VE-Cadherin-expressing cells were labelled, allowing cellular tracking of ECs fate in the adult skeletal muscle. To deplete circulating monocytes and reduce MP infiltration, 60-days-old mice were intravenously injected with liposomes containing Clodronate (CLL) or PBS as a control (SHAM). Intravenous injections of CLL were performed one day before and two days after cardiotoxin (CTX) damage on quadriceps muscles to ensure a steady MP depletion throughout regeneration. Based on our previous data, in these experimental conditions, ECs are undergoing EndMT 5 days post-injury[8]. Therefore, at this time point, muscles were collected and processed for analysis. A total of 6 mice were employed and divided into the two experimental groups (Supplementary Fig. 1A). To confirm an effective reduction of circulating monocytes in CLL vs SHAM-treated mice, peripheral blood was collected 4 days after CTX injection. Flow cytometric analysis showed a significant depletion of CD45$^+$ CD11b$^+$F4/80$^+$ circulating phagocytes, which were less frequent in CLL-treated than in SHAM-treated animals ($7.9 \pm 0.5\%$ vs $3.3 \pm 0.2\%$, respectively, $P < 0.01$, $n = 3$; Supplementary Fig. 1B). Quadriceps muscles were then collected, dissociated into single-cell suspensions, processed on the 10x Chromium Genomics platform and sequenced (Illumina). The Seurat package was used for single-cell RNA-sequencing (scRNA-seq) data filtering and processing. After filtering, the scRNA-seq dataset contained 33,935 cells (SHAM = 18,336, CLL = 15,599), expressing a total of 22,296 different genes (GEO database under accession code GSE291782). Experimental replicates generated from different mice ($n = 3$) presented only minor differences, most notably a variation in the incidence of mesenchymal population in the SHAM9 sample, suggesting that the datasets contained minimal batch effects and mouse-to-mouse variability (Supplementary Fig. 2A–D). Therefore, for subsequent analyses, biological replicates were combined and integrated to improve cell sample size and statistical power.

Uniform manifold approximation and projection (UMAP) and t-distributed stochastic neighbour embedding (t-SNE) were used to visualize the embedding of the integrated scRNA-seq dataset (Fig. 1A, C). Unsupervised clustering resulted in 35 different clusters across the 6 samples. Clusters were next labelled and merged based on canonical skeletal muscle gene expression markers, obtaining a total of 14 (Fig. 1B). The top 5 marker genes of each cluster are shown in Supplementary Fig. 2D. MuSCs and myoblasts formed a cluster marked by the expression of *Pax7* and *Myod1*, while mature myocytes formed a distinct one expressing *Myh1* (myosin heavy chain 1) and *Acta1* (skeletal muscle alpha actin 1). ECs were marked by the expression of *Cdh5* (VE-Cadherin) and *Pecam1* (CD31), while a cluster of pericytes and smooth muscle cells expressed *Rgs5* and *Pdgfrb*. We were also able to identify a cluster marked by the expression of *Mpz* that corresponds to Schwann cells (neural) and another that expressed *Adipoc* and *Plin1* representing adipocytes. Immune cells formed several discrete clusters that represent the main immune populations described to be present 5 days post-injury[12]. B, T, and NK cells were grouped for simplicity and were marked by the expression of *Ptprc* (CD45), *Flt3* and *Ccl5*. Neutrophils were identified as expressing *S100a8* and *S100a9*. Mast cells by *Cpa3* and *Cma1* and dendritic cells were marked by the expression of *Cd209a* and *Cd74*. MPs formed the largest cluster of immune cells marked by *Adgre1* (F4/80), *Aif1* and *Csf1r* expression. In addition, a population of mesenchymal cells containing tenocytes expressing *Scx* and *Tnmd*, and FAPs expressing *Pdgfrα* formed another cluster. Interestingly, we were able to identify a cluster of cells recently described as immunomyoblasts[13] that expressed both immune (*C1qa, C1qb, H2-Eb1, H2-Aa*) and myogenic genes (*Pax7, Myf5*) (Fig. 1B, Supplementary Fig. 2E). The cell populations present in our experiment are consistent with previously published literature[12,13], suggesting that our data recapitulates key events in skeletal muscle regeneration. Nonetheless, differences in cellular composition of the regenerating muscle niche were evident between mice treated with SHAM and those treated with CLL.

As expected, the composition of immune cell subsets was altered in CLL-treated mice compared with SHAM controls (Fig. 1D, Supplementary Fig. 1C, Table S1). MPs, the predominant immune population during muscle regeneration, were the most affected in terms of overall size reduction, decreasing from 35.77% to 15.26% (Fig. 1D, Supplementary Fig. 1C, Supplementary Data 1). Dendritic cells were also reduced (3.71% vs 1.4%), as were immunomyoblasts (2.35% vs 0.43%) (Fig. 1D, Supplementary Fig. 1C, Supplementary Data 1). In contrast, adaptive immune populations, including B, T, and NK cells (5.33% vs 4.6%), as well as neutrophils (0.25% vs 0.33%), showed minimal variation between conditions (Fig. 1D, Supplementary Fig. 1C, Supplementary Data 1), suggesting that CLL treatment preferentially impacts highly phagocytic populations rather than inducing a generalized immune depletion.

In parallel, we observed a marked reduction in ECs (10.68% vs 2.83%) together with an expansion of mesenchymal populations, primarily driven by FAPs (23.93% vs 58.16%) (Fig. 1D, Supplementary Fig. 1C, Supplementary Data 1), indicating a substantial reshaping of the regenerative niche.

The impact of an impaired muscle regenerating niche on MuSCs and FAPs

A delay in myogenesis resulting from the partial depletion of MPs in *Tibialis anterior* (TA) and triceps muscles was demonstrated in previously published data from our group, with histological analysis of muscles 5 days post injury already exhibiting differences in cellular organization and composition[8]. Similar histological differences were consistently observed in cross sections of the quadriceps of CLL-treated mice (Supplementary Fig. 1D) and align with the shifts observed in the cellular composition in our scRNA-seq dataset (Fig. 1D).

Since MuSCs are the primarily responsible for the development of new muscle fibres, we conducted sub-clustering on a total of 2967 MuSCs to investigate potential alterations in their subpopulations that could explain this delay in myogenesis. We identified three distinct clusters of MuSCs (Fig. 2A, B), a quiescent subpopulation marked by *Pax7* expression, activated/dividing MuSCs expressing *Pax7, Myod1*, and *Cdk1*, and committed MuSCs marked by *Myog* expression (Fig. 2A). All of them were negative for the mature myocyte marker *Myh1* (Fig. 2A). The different MuSC states presented variations in proportions between our two experimental conditions, with CLL-treated mice showing a lower percentage of quiescent MuSCs (75.4% vs. 64.4%), higher percentage of activated MuSCs (9.8% vs. 17.8%), and a similar proportion of committed MuSCs (14.8% vs. 17.8%) (Fig. 2C). These findings suggest that MP depletion results in a continuous activation of quiescent MuSCs, possibly due to aberrant signalling from the surrounding regenerative niche, which is essential for their commitment to myocytes or their return to the quiescent pool.

Next, we sought to understand the biological processes underlying the higher proportion of FAPs observed in the CLL condition. For this, we subjected the FAP population, consisting of a total of 13,837 cells (Fig. 2D), to differential gene expression (DGE) analysis followed by gene set enrichment analysis (GSEA), querying the Gene Ontology (GO) Biological Process and KEGG databases. Recent studies have demonstrated that

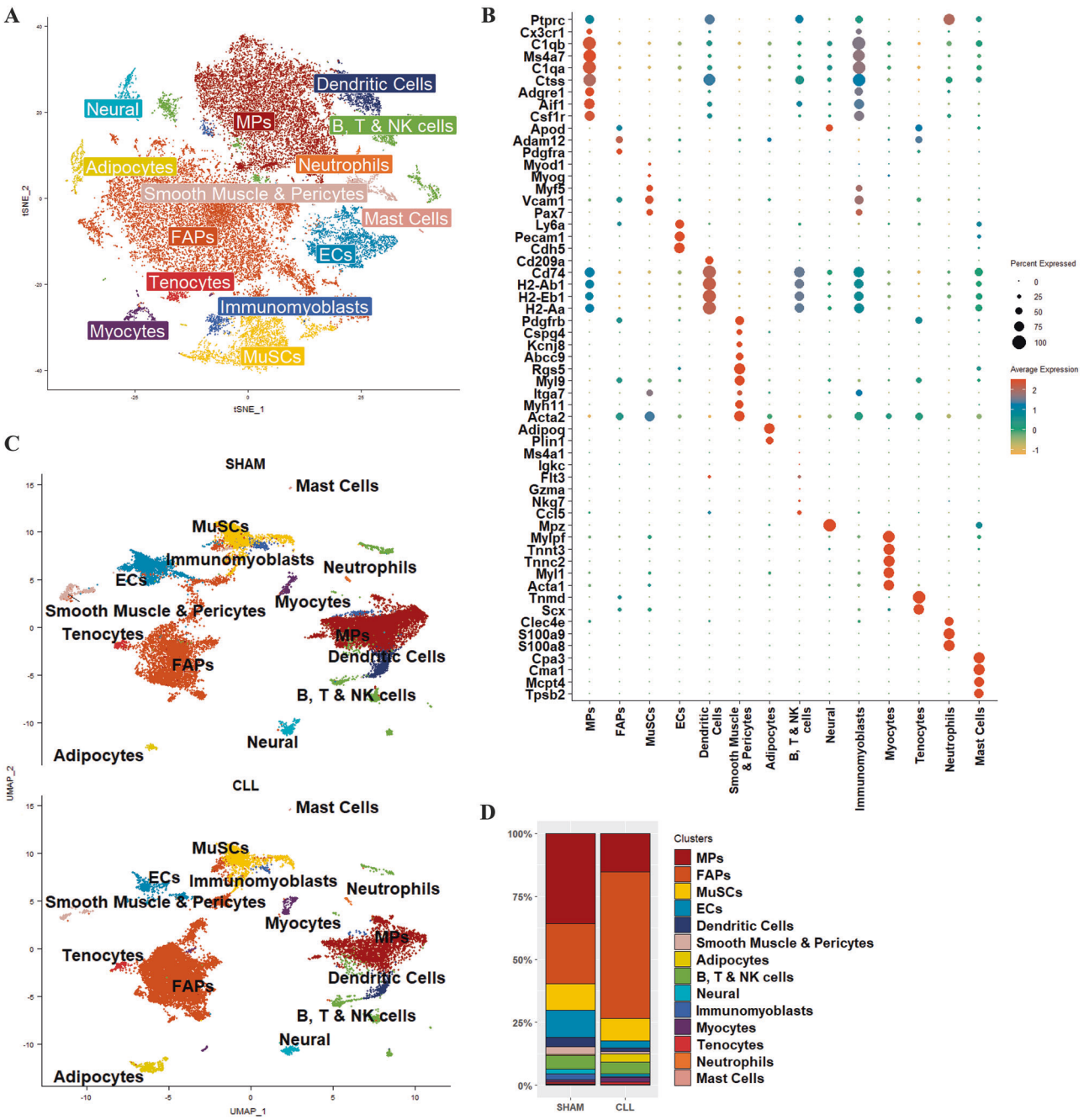

Fig. 1 | Single-Cell RNA sequencing reveals cellular heterogeneity in the muscle regenerating niche of Clodronate-treated (CLL) and Control (SHAM) *Cdh5-CreER^{T2}:R26R-tdTomato* mice. A t-SNE embedding of both experimental conditions (Clodronate-treated (CLL) and Control (SHAM) *Cdh5-CreER^{T2}:R26R-tdTomato*) coloured by individual cluster identities and manually annotated based on canonical skeletal muscle marker gene expression. **B** DotPlot demonstrating cell-type marker gene expression used for meta-cluster classification. Dot size indicates the percentage of cells expressing each gene, and dot colour represents the average expression level. **C** UMAP embedding of all sequenced samples. **D** Relative proportion and frequency of cell types per experimental condition.

traditional scRNA-seq DGE methods display an inferior performance when compared to pseudo-bulk approaches in the presence of biological replicates, as they focus on individual cell differences and do not account for inter-individual variation[14,15]. Given that our experimental scheme included three biological replicates, and our focus is on the impact of our experimental condition rather than biological variability, we employed a pseudo-bulk approach using the DESeq2 package (Supplementary Data 2).

GSEA results revealed that when MP recruitment is impaired, FAPs exhibit activation of the glycolytic and pentose phosphate pathways, indicating increased anabolic metabolism at this time point compared to normal regenerative conditions (Fig. 2E, Supplementary Data 3). The activation of carbon metabolism emphasizes an increased energy demand in FAPs under the CLL condition, while the activation of DNA replication sustains enhanced proliferative activity (Fig. 2E). Indeed, a metabolic shift towards glycolysis is commonly associated with higher proliferation rates, as it provides a faster means of energy production, and is further supported by the activation of HIF-1 signalling (Fig. 2E), a pathway active under hypoxic conditions and described to promote glycolysis. Such metabolic state dysregulations have been equally observed in FAPs under pathological conditions, where it is linked to an increased fibrogenic potential[16], and under dystrophic conditions, where it correlates with higher FAPs proliferation and adipogenic differentiation rates[17].

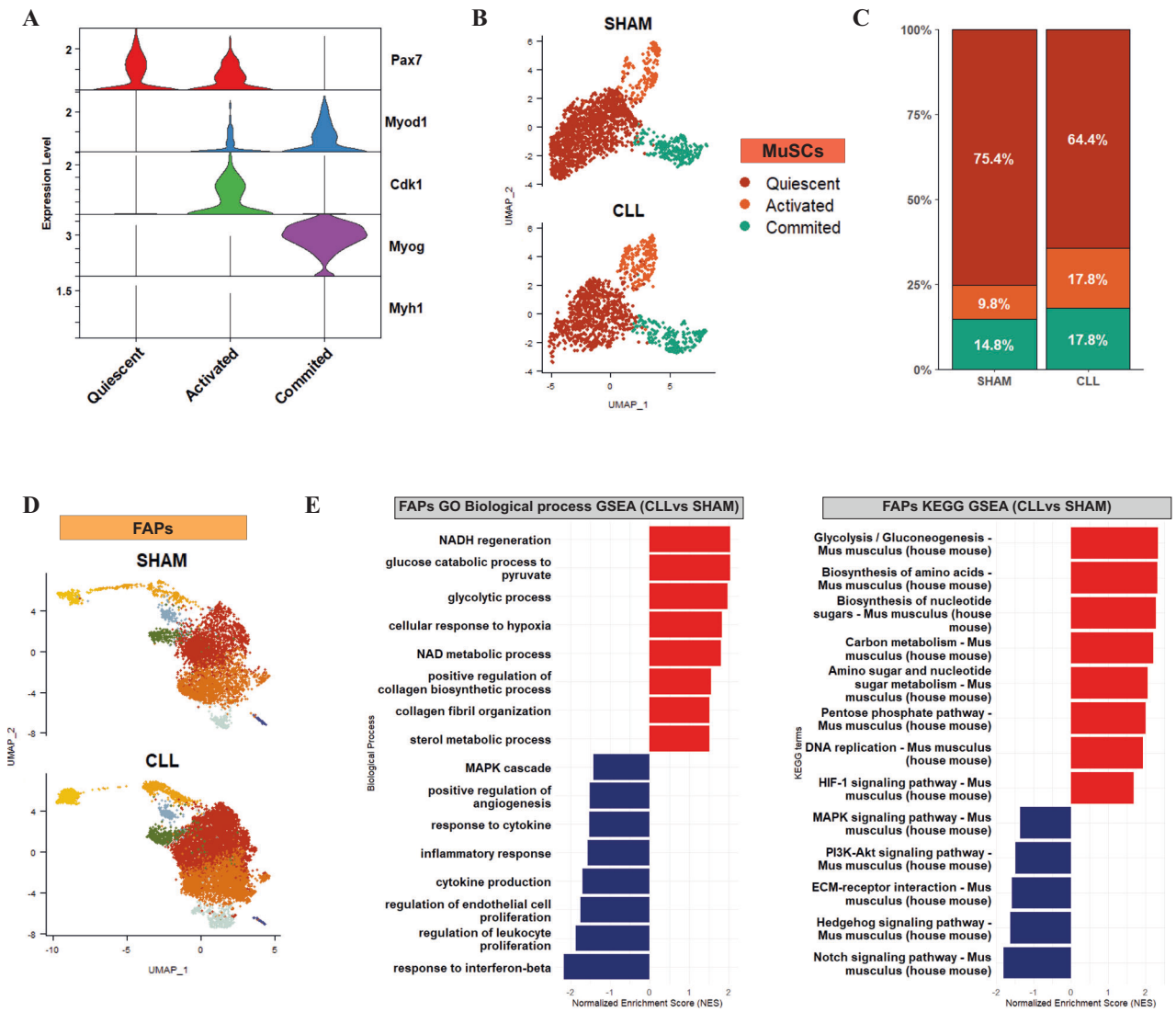

Fig. 2 | Impact of the defective muscle regenerative microenvironment driven by compromised MP infiltration on MuSCs and FAPs subsets. A Violin Plot showing normalized and log-transformed expression of MuSCs subpopulations specific genes. **B** UMAP plot of MuSCs subclustering split per experimental condition. **C** Relative proportion of MuSCs subpopulations per experimental condition. **D** UMAP embedding of FAP population split per experimental condition. **E** BarPlot showing selected GO biological process and KEGG-terms gene set enrichment analysis (GSEA) comparing CLL vs SHAM conditions, in FAPs. The Normalized Enrichment Score (NES) indicates the degree of enrichment for each gene set. Positive NES values (in red) represent pathways activated in CLL, while negative NES values (in blue) represent pathways suppressed in CLL.

In the CLL condition, FAPs also display enhanced collagen biosynthesis, alongside suppression of inflammatory response and of EC proliferation/angiogenesis regulation (Fig. 2E). The suppression of Notch and Hedgehog signalling (Fig. 2E) suggests similar higher FAP adipogenic differentiation, as these pathways have been proven to negatively regulate FAP proliferation and adipogenic differentiation both in vitro and in vivo[18,19].

Together, these findings indicate that a deficiency in MP recruitment dynamics affects the correct onset of repair and contributes to both the sustained activation and impaired resolution of FAPs, mirroring changes reported in dystrophic contexts.

Compromised MP infiltration contributes to ECs' phenotypic switch and upregulation of TGF-β signalling pathway genes

Previous work from our group has demonstrated that compromised MP infiltration during skeletal muscle regeneration triggers ECs to undergo EndMT, contributing to the uncontrolled expansion of fibroblast/mesenchymal cells[8]. However, ECs-specific transcriptional changes remained unexplored. To address this gap, DGE analysis (Supplementary Data 4) was conducted on the EC subsets across experimental conditions, followed by GSEA analyses (Supplementary Data 5).

The GSEA analysis revealed that, in CLL-treated mice, ECs exhibit suppression of endothelial cell differentiation and angiogenesis (Fig. 3A), as sustained by the consistent significant downregulation of key EC markers (*Cdh5, Pecam1, Vwf, Kdr*, and *Tie1*) across all sequenced biological samples (Fig. 3D). In addition, the activation of Hippo signalling and the concurrent suppression of the Notch signalling pathway (Fig. 3A, B) suggest altered angiogenesis. The activation of Hippo signalling in ECs inhibits the transcriptional coactivator YAP (Yes-associated protein 1). YAP, known for its influence on the expression of genes regulating cell proliferation, survival, and differentiation, plays a pivotal role in vasculogenesis and angiogenesis[20–22]. On the other hand, Notch signalling is essential for vascular stabilization and differentiation of the emerging vascular tree by inhibiting ECs proliferation and promoting the stabilization of cell–cell junctions[23,24].

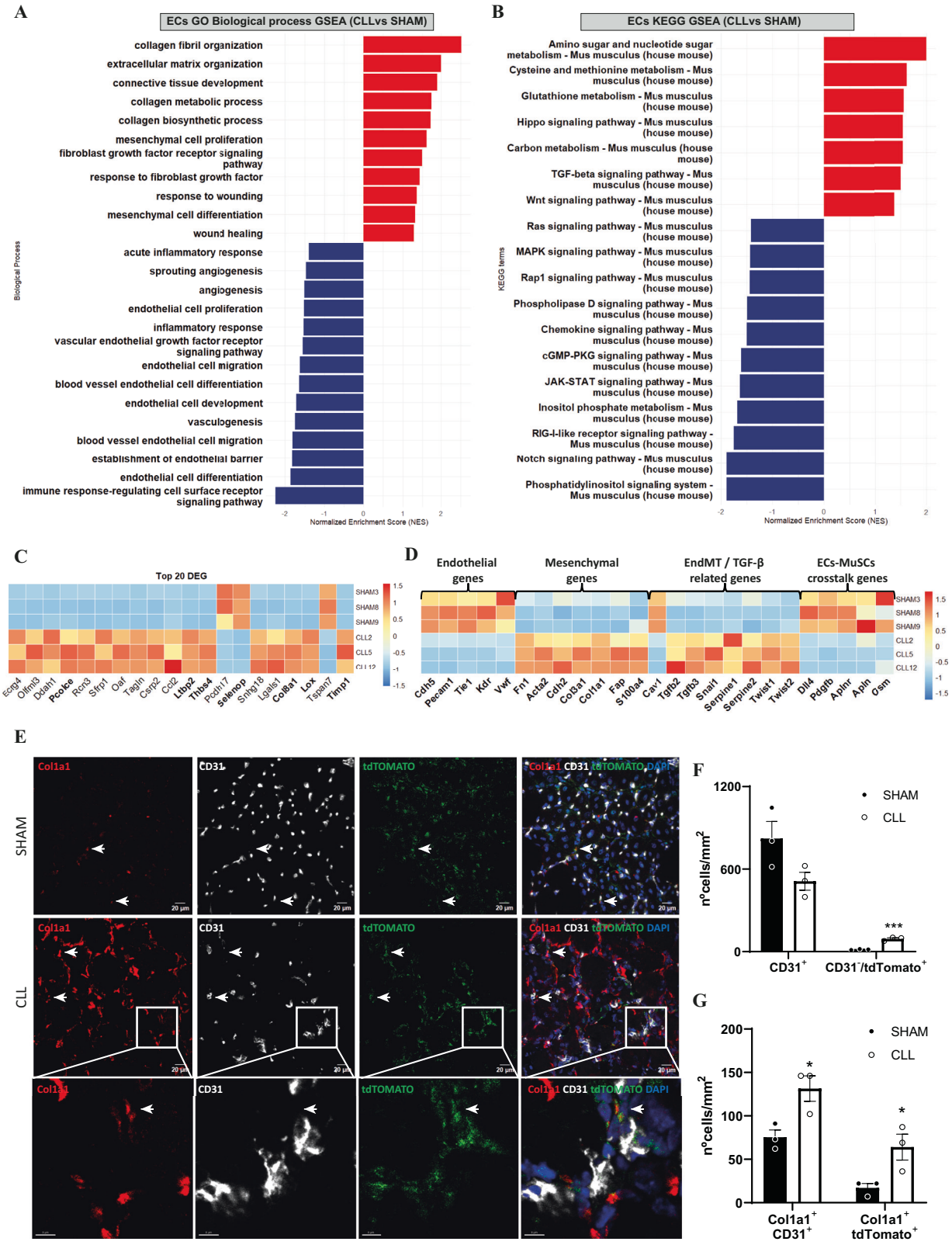

At the same time, ECs in CLL-treated regenerating muscles display activation of pathways associated with mesenchymal cell differentiation, fibroblast proliferation and ECM production (Fig. 3A). This is related to the significant up-regulation of mesenchymal genes such as *Acta2* (αSMA), *Cdh2* (N-cadherin), *Fn1* (fibronectin), *S100A4* (FSP-1), and different collagen types (Fig. 3D), with the presence of ECM-related genes among the top 20 significant DEGs (Fig. 3C).

Immunostaining on muscle sections of *Cdh5-CreER^{T2}:R26R-tdTomato* mice confirmed the reduction in the EC population in CLL-treated mice in comparison to the control (822 ± 124 CD31$^+$ cells/mm^2 vs 511 ± 65 CD31$^+$

Fig. 3 | Impaired MP recruitment results in endothelial cells undergoing transcriptional and phenotypic changes in regenerating muscles. A BarPlot showing the top dysregulated processes from the Gene set enrichment analysis (GSEA) (GO biological process) related to immune response, ECM and endothelial functions in ECs from CLL *Cdh5-CreER^{T2}:R26R-tdTomato* treated mice. The Normalized Enrichment Score (NES) indicates the degree of enrichment for each gene set. Positive NES values (in red) represent pathways activated in CLL, while negative NES values (in blue) represent pathways suppressed in CLL. **B** BarPlot showing the dysregulated pathways from the GSEA (KEGG database) in ECs from CLL *Cdh5-CreER^{T2}:R26R-tdTomato* treated mice. The Normalized Enrichment Score (NES) indicates the degree of enrichment for each gene set. Positive NES values (in red) represent pathways activated in CLL, while negative NES values (in blue) represent pathways suppressed in CLL. **C** Heatmap showing the expression of the Top 20 differentially expressed genes (DEG) of the 3626 DE genes assessed by DEseq2, P < 0.05. Bold genes are related to ECM turnover. **D** Heatmap of the main endothelial, mesenchymal, EndMT-related genes and ECs-MuSCs crosstalk, differentially expressed between conditions. **E** Immunofluorescence staining of quadriceps muscle cross-sections of SHAM- and CLL-treated *Cdh5-CreER^{T2}:R26R-tdTomato* mice 5 days after CTX injection for ECs (CD31, white), tdTomato (green), Col1a1 (red) and nuclear marker (DAPI, blue). White arrows indicate examples of CD31$^+$ or tdTomato$^+$ cells expressing Col1a1. Magnification 40x, Scale bar at 20 μm and amplified images at 8 μm. **F** Quantification of CD31$^+$ and CD31$^+$/tdTomato$^+$ cells per square millimetre in quadriceps muscle cross-sections of SHAM- and CLL-treated *Cdh5-CreER^{T2}:R26R-tdTomato* mice 5 days after CTX injection ($n = 3$, with three representative sections of the muscle examined). Statistically significant differences are indicated as *** representing $P < 0.001$, CD31$^+$ $P = 0.0902$ (two-tailed unpaired Student's *t*-test). **G** Quantification of CD31$^+$Col1a1$^+$ and tdTomato$^+$Col1a1$^+$ cells per square millimetre in quadriceps muscle cross-sections of SHAM- and CLL-treated *Cdh5-CreER^{T2}:R26R-tdTomato* mice 5 days after CTX injection ($n = 3$, with three representative sections of each muscle examined). Statistically significant differences are indicated as * representing $P < 0.05$ (two-tailed unpaired Student's *t*-test).

cells/mm^2, SHAM vs CLL respectively, $P < 0.0913$, Fig. 3F, Supplementary Fig. 3). ECs exhibited different morphology and distribution patterns in the two experimental conditions, being uniformly shaped and regularly distributed throughout the regenerative area in controls, whereas in CLL-treated animals their morphology was elongated and their distribution appeared irregular, occasionally clustering together resembling small niches (Fig. 3E, and Supplementary Fig. 3A). Indeed, vessel quantification analysis showed a significant reduction in both CD31$^+$vessel number and total CD31$^+$vascular area in the muscles of CLL-treated mice compared with SHAM controls (Vessels n/ROI 82 ± 4 vs 37 ± 3 SHAM vs CLL respectively, $P < 0.001$) (CD31$^+$ Area μm^2/ROI 6932 ± 299 vs 3341 ± 466, SHAM vs CLL respectively, P < 0.001) (Supplementary Fig. 3B, C). Subset analysis of vessel cross-sectional morphology based on particle roundness (Supplementary Fig. 3D) showed that round vessel cross-sections are characterized by a homogeneous and small physiological diameter in both experimental conditions but are less abundant in CLL-treated mice (round vessels n/ROI: 56.32 ± 4 vs 27.12 ± 4, SHAM vs CLL, $p < 0.05$) (Supplementary Fig. 3E). Moreover, the large-vessel compartment was particularly affected in CLL treated mice, with a reduction in large-vessel total area (3679 ± 453 vs 1975 ± 612 μm², SHAM vs CLL, $P < 0.05$) and a trend toward a lower fraction of large vessels (23 ± 3% vs 15 ± 2%, SHAM vs CLL, $P > 0.05$) (Supplementary Fig. 3F, G). Furthermore, in the CLL-treated condition the lineage tracing label tdTomato was detected in a significantly higher subset of cells not marked by CD31 (15 ± 2 cells/mm^2 vs 92 ± 8 cells/mm^2, SHAM vs CLL respectively, $P < 0.001$, Fig. 3F, Supplementary Fig. 3B). Likewise, Col1a1, the main component of fibrotic ECM and a significant upregulated gene on ECs DEG analysis (Fig. 3D), showed a higher number of cells expressing this ECM protein in the immunostained muscles of CLL-treated mice (Fig. 3E), including both CD31$^+$ cells (75 ± 8 cells/mm^2 vs 131 ± 15 cells/mm^2, P < 0.05, Fig. 3E, G) and tdTomato$^+$ cells (17 ± 5 cells/mm^2 vs 64 ± 15 cells/mm^2, $P < 0.05$, Fig. 3E, G).

Another significant observation in this context was the activation of TGF-β signalling (Fig. 3A, B), a pathway well-recognized as a driver of EndMT in various tissues and pathological conditions[25–27]. This activation is evidenced by the significant upregulation of key TGF-β-associated transcription factors, including *Snai1*, *Twist1*, *Twist2*, and *Serpine1* (PAI-1), as well as increased expression of *TGF-β2* and *TGF-β3* isoforms (Fig. 3C). Further corroborating the involvement of TGF-β signalling in skeletal muscle EndMT is the suppression of phosphatidylinositol signalling (Fig. 3B), which is known to mediate angiogenesis and VEGF expression[28], and to inhibit TGF-β-induced EndMT in bone marrow-derived endothelial progenitor cells[29]. These observations are consistent with our previously published findings, which demonstrated elevated TGF-β/SMAD signalling in endothelial-derived progenitors in the absence of MPs seven days post-injury[8].

Several genes - *Dll4, Pdgfb, Aplnr, Apln*, and *Osm* (Fig. 3D) - known to play crucial roles in the interaction between myogenesis and angiogenesis[30–32] were found to be significantly downregulated in ECs from CLL-treated mice. These findings, combined with the observed reduction in quiescent MuSCs and concomitant increase in activated MuSCs (Fig. 2C) suggest that disrupted crosstalk with ECs could hamper the ability of MuSCs to commit to myocyte differentiation and/or return to the quiescent pool[31]. Furthermore, the suppression of immune and inflammatory responses (Fig. 3A), implies that EC dysfunction similarly affects ECs and immune cells interaction.

Taken together, these findings suggest that MP depletion in regenerating muscles results in transcriptional and phenotypic alterations in ECs. The perturbation of MP recruitment triggers EndMT through TGF-β signalling pathway activation, which impairs ECs function. These changes adversely affect the regenerative microenvironment by impairing angiogenesis, myogenesis and immune response, highlighting their interconnection during muscle repair.

Macrophages exhibit a dysregulated transcriptomic profile upon impaired recruitment following muscle injury

MPs are highly plastic cells with the ability to acquire different inflammatory phenotypes and functions depending on their origin and tissue microenvironment, expressing a specific gene signature representative of each specialized function during the different phases of muscle repair[5]. To investigate MP heterogeneity between experimental conditions, we subjected the MP population, consisting of a total of 8,940 cells, to unsupervised clustering. This analysis revealed seven clusters (Fig. 4A), which were subsequently merged and classified into four subtypes based on their top marker gene expression profile (Fig. 4B).

The Inflammatory MP cluster was characterized by genes related to interferon signalling (*Ifitm3, Ifit3, Irf7, Ifit2*), commonly associated with pro-inflammatory activity. The ECM-related MP cluster expressed genes involved in collagen regulation and ECM remodelling (*Dcn, Col5a2, Serpinh1*). The Proliferating MP cluster exhibited genes linked to cell division, cytoskeletal dynamics, and intracellular transport (*Stmn1, Tubb5, Birc5, Tuba1b, Ran*). The MP subtype identified expressed MHC II genes (*H2-Ab1, H2-Aa, H2-Eb1*) and typical M2 markers, including *Mrc1* (Cd206), *Cd163*, and *Gpnmb*, and was classified as M2-like MPs (Fig. 4C). All clusters were positive for *Adgre1* (F4/80) and *Cx3cr1* and negative for dendritic cell markers *Flt3* and *Cd209a* (Supplementary Fig. 4A), supporting their MP identity. These populations resembled MP subtypes recently described during skeletal muscle regeneration[33–35]. A slight difference in MP composition was observed between conditions, with CLL-treated mice presenting a lower percentage of Inflammatory (3,92% vs 1,13%) and M2-like MPs (86,14% vs 79,21%) and a higher one of Proliferating (1,65% vs 7,18%) and ECM-related MPs (8,29% vs 12,47%) (Fig. 4C).

Given the crucial role of M2-like MPs in orchestrating the regenerative process[2] and to understand what underlying functions and mechanisms could be dysregulated and impacting the regenerative environment, we conducted DGE and GSEA analysis within this subset (Supplementary Data 6, 7).

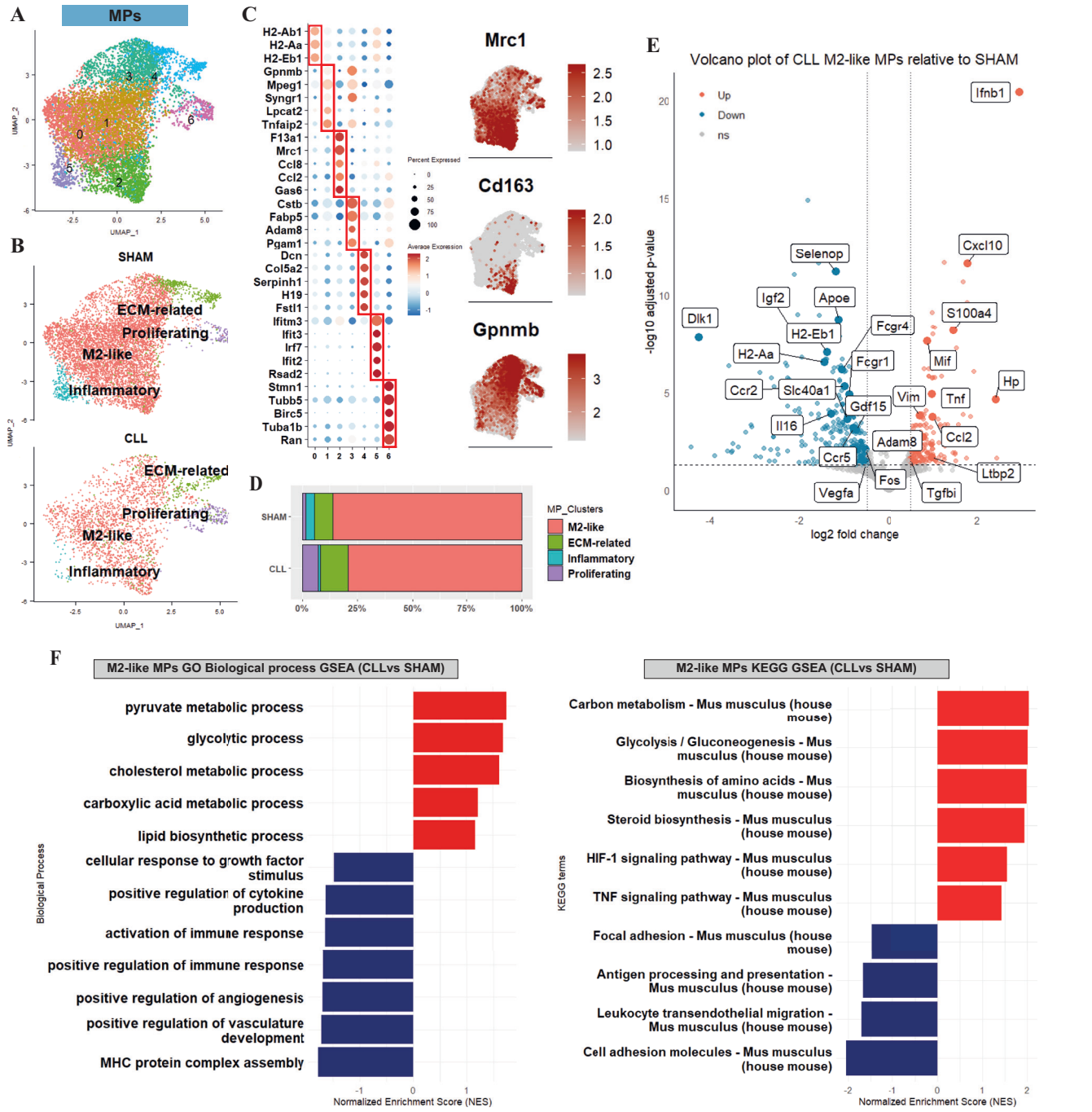

Fig. 4 | Transcriptomic analysis of MPs in the muscle regenerating niche reveals dysregulated profiles upon compromised MP infiltration. A UMAP plot of MPs sub-clustering. **B** Labelling of cells based on the top-expressed marker genes. **C** DotPlot of the top 5 expressed genes for each sub-cluster and FeaturePlot showing the normalized expression of M2- like specific genes Mrc1 (*Cd206*), *Cd163* and *Gpnmb* to highlight the sub-clustering of MPs. Dot size indicates the percentage of cells expressing each gene, and dot colour represents the average expression level. **D** Relative proportion of MP subpopulations per condition. **E** Visualization by a Volcano plot of the statistically significant gene expression changes (fold change ≥1.5 and adjusted *P* value < 0.05) of M2-like MPs between conditions. Upregulated genes are labelled in red and downregulated genes labelled in blue. **F** BarPlot showing selected GO biological process and KEGG-terms gene set enrichment analysis (GSEA) comparing CLL vs SHAM conditions, in M2-like MPs. The Normalized Enrichment Score (NES) indicates the degree of enrichment for each gene set. Positive NES values (in red) represent pathways activated in CLL, while negative NES values (in blue) represent pathways suppressed in CLL.

Under normal repair conditions, at the observed time point, MPs should have already polarized towards an anti-inflammatory/pro-regenerative phenotype, characterized by oxidative phosphorylation and glutamine metabolism together with pro-angiogenic and reparative functions[5,35]. However, in CLL-treated mice, MPs displayed higher activation of pathways typically associated with a pro-inflammatory state, including glycolysis, HIF-1α pathway, and TNF signalling (Fig. 4F). Furthermore, MPs in CLL mice presented an activation of cholesterol metabolic process and lipid biosynthetic process (Fig. 4F).

Key genes associated with the anti-inflammatory and pro-regenerative response, including *Gdf15, Apoe, Selenop, Fos, Ccr5*, and *Igf2*, were significantly downregulated, whereas inflammatory genes such as *Ifnb1, Hp, Cxcl10, Tnf, Ccl2, Vim, Tgfbi*, and *Ltbp2* were significantly upregulated (Fig. 4E). Although not statistically significant, well-established cytokines

associated with MP inflammatory profile exhibited altered expression patterns. *Il1b* and *Cd86*, markers of inflammatory MPs, showed higher average expression in the CLL condition, as did *Tgfb1* and *Il10* - markers of anti-inflammatory MPs[36] (Fig. S4B). In addition, MP-derived *Igf1*, a factor crucial for resolving inflammation and driving MP polarization[37], was downregulated (Supplementary Fig. 4B).

GO biological process analysis further indicated the suppression of immune response- and angiogenesis-related processes (Fig. 4F) with *Vegf*, a fundamental cytokine produced by MPs to induce angiogenesis, exhibiting a significant downregulation (Fig. 4E).

Taken together, these findings suggest that impaired MP recruitment during muscle regeneration disrupts MP polarization and sustains a pro-inflammatory state, which may in turn affect the resolution of inflammation by impairing key regenerative processes such as angiogenesis, myogenesis, and ECM remodelling, ultimately compromising muscle repair and acting as a trigger on ECs phenotypic switch.

Interactions between macrophage ligands and endothelial cells receptors identifies intercellular communication influencing endothelial cells behaviour

The cytokines and growth factors released by MPs can prompt different cellular responses. Thus, to address the impact of dystrophic MPs on EC fate decisions, we conducted CellChat analysis focusing on secreted signalling where MPs served as sources and ECs as targets (Supplementary Data 8).

The first striking observation was the presence of a higher number of interactions in the CLL condition compared to the control (Fig. 5A). Among these interactions, TNF exhibited increased interaction probability (Fig. 5B, Supplementary Fig. 5A), consistent with results from DGE and GSEA analysis (Fig. 4E-F). Moreover, interactions dependent on another cytokine, osteopontin (SPP1), were exclusively detected in the CLL condition (Fig. 5A, Supplementary Fig. 5A). Conversely, the interaction probability associated with growth differentiation factor 15 (GDF15), a gene previously identified as downregulated in the MP DGE analysis (Fig. 4E), was reduced in CLL-treated mice compared to SHAM (Fig. 5B, Supplementary Fig. 5A). This was an interesting finding as recent literature describes SPP1 and TNF as pro-inflammatory cytokines involved in TGF-β signalling[38–40], while GDF15 has been recognized as a key MP-derived factor in orchestrating the pro-regenerative phase during muscle repair[41]. Therefore, our results identified TNF, SPP1, and GDF15 as potential key upstream signals driving MPs and ECs crosstalk during generation and hinted at their interaction with the TGF-β pathway at the onset of EndMT in the muscle.

The analysis of signalling pathway information flow across conditions revealed an enrichment of TGF-β, TNF, and SPP1, along with a reduction in GDF signalling in CLL-treated mice. These findings further suggest a compromised transition from a TNF-rich to a TGF-β-rich environment, characterized by overlapping cytokine signalling and the presence of a microenvironment with elevated pro-inflammatory signals and diminished regenerative cues (Supplementary Fig. 5B).

To validate CellChat findings, we performed immunostaining for F4/80 and SPP1 (Fig. 5C). We detected a reduced number of F4/80$^+$ cells in the CLL condition (1264 ± 257 cells/mm^2 vs 674 ± 81 cells/mm^2, SHAM vs CLL respectively, $P < 0.094$, Fig. 5D) while SPP1 expression displayed a broader distribution and a significantly higher proportion of SPP1$^+$ MPs in CLL-treated mice (29 ± 1% vs 50 ± 5%, SHAM vs CLL respectively, $P < 0.05$, Fig. 5E), thus aligning with our scRNA-seq results.

In addition to MPs, SPP1 protein expression was observed in non-MP cells (Fig. 5C). Thus, we examined *Spp1* gene expression across the major cell populations in our scRNA-seq dataset. Consistently, CLL-treated mice showed elevated *Spp1* gene expression not only in MPs but also in FAPs, MuSCs, and ECs (Fig. 5F). In contrast, under control conditions, *Spp1* expression was restricted to MPs, MuSCs, and myocytes. Immunostaining analysis for SPP1 and PDGFRα confirmed that indeed a subset of FAPs expressed SPP1 in CLL-treated muscles (Supplementary Fig. 5D). However, CellChat analysis using FAPs as signalling source and ECs as targets did not identify SPP1-dependent interactions (Supplementary Fig. 5E), suggesting that although FAPs can express SPP1, they are an unlikely source of SPP1-mediated signalling toward ECs in this context.

Further analysis of signalling genes revealed that in CLL-treated mice, MPs, FAPs, MuSCs, ECs, and myocytes exhibited higher expression of TGF-β isoforms, particularly *Tgf-β2* and *Tgf-β3*, whereas *Tnf* and *Gdf15* expression remained exclusive to MPs. In ECs, CellChat analysis reported that SPP1 signalled through the receptor CD44 and integrin heterodimer receptors (ITGB1, ITGB5, and ITGAV) (Fig. 5B, Supplementary Fig. 5A). Besides the expression of *Itgb1*, the expression of all other SPP1 receptors was exclusively observed in the CLL condition (Supplementary Fig. 5C), further emphasizing the potential negative influence of elevated SPP1 expression on EC behaviour during impaired MP recruitment conditions.

Overall, our data show that the pro-inflammatory state caused by reduced MP recruitment during muscle regeneration results in altered cytokine expression patterns and disruption in the MP-EC interactions, pointing to a key role of SPP1 and identifying potential regulatory mechanisms impacting ECs phenotypic fate.

TGF-β and SPP1 synergize to promote EndMT in vitro

Given the established roles of TGF-β and SPP1 in promoting fibrosis during muscular dystrophy, and to further investigate their link to EndMT[38,42], we cultured mouse skeletal muscle ECs (mECs)[43] with TGF-β and/or SPP1 during a period of 3 and 5 days (Supplementary Fig. 6A).

TGF-β-treated mECs exhibited a clear morphological transition from the characteristic cuboidal shape observed in the control group (medium without TGF-β or SPP1) to a more elongated, spindle-like phenotype at both 3 days (Supplementary Fig. 6B) and 5 days (Fig. 6A). Gene expression analysis confirmed this phenotypic change, showing a significant decrease in the endothelial marker *Cd31*, along with an increase in the transitional EndMT marker *Snail*, *PAI-1*, and the mesenchymal marker *αSMA* in TGF-β-treated ECs at both time points (Fig. 6B, Supplementary Fig. 6C).

In contrast, treatment with SPP1 alone did not induce significant changes in cell morphology. However, a reduction in VE-Cadherin gene expression was observed at day 3 (Supplementary Fig. 6C), with a significant decrease compared to the control group at day 5 (Fig. 6B). Interestingly, the combination of SPP1 and TGF-β yielded the most striking results. ECs treated with both factors displayed a morphological transition similar to that seen with TGF-β alone at 3 and 5 days (Fig. 6B, Supplementary Fig. 6C), but with significantly lower expression of *Cd31* and *VE-Cadherin* after 3 days and significantly higher expression of the transitional EndMT markers *Snai1* and *PAI-1* after 5 days of treatment (Fig. 6B).

These findings further strengthen the evidence that TGF-β signalling plays a key role in EndMT within skeletal muscle. Moreover, they suggest that SPP1 alone can affect *VE-Cadherin* expression in ECs and, when combined with TGF-β, exert a synergistic effect that enhances the expression of transcription factors associated with EndMT. This highlights the role of SPP1 in mediating the crosstalk between MPs and ECs, thereby influencing EC phenotypic fate.

Osteopontin inhibition in vivo ameliorates the onset of EndMT after muscle injury

To further assess in vivo the role of SPP1 during skeletal muscle regeneration under dystrophic conditions, CLL-treated mice were administered an osteopontin inhibitor (OPN-IN-1 or OPNi). Following CTX-mediated muscle injury, mice received an intraperitoneal injection of OPNi or vehicle on the day, and a second OPNi or vehicle injection three days after injury (3 mice per group). Muscles were then collected for analysis 5 days following CTX injection.

Immunostaining analysis of F4/80$^+$ cells showed that OPN inhibition did not significantly affect the total number of MPs present on regenerating muscles (527.6 ± 63.8 cells/mm^2 vs 526.8 ± 101.2 cells/mm^2, Vehicle vs OPNi, respectively, $P > 0.05$, Supplementary Fig. S7B). However, the percentage of MPs expressing SPP1 was significantly reduced in OPNi-treated mice compared with vehicle-treated controls (38.3 ± 5% vs 16.5 ± 1.6%,

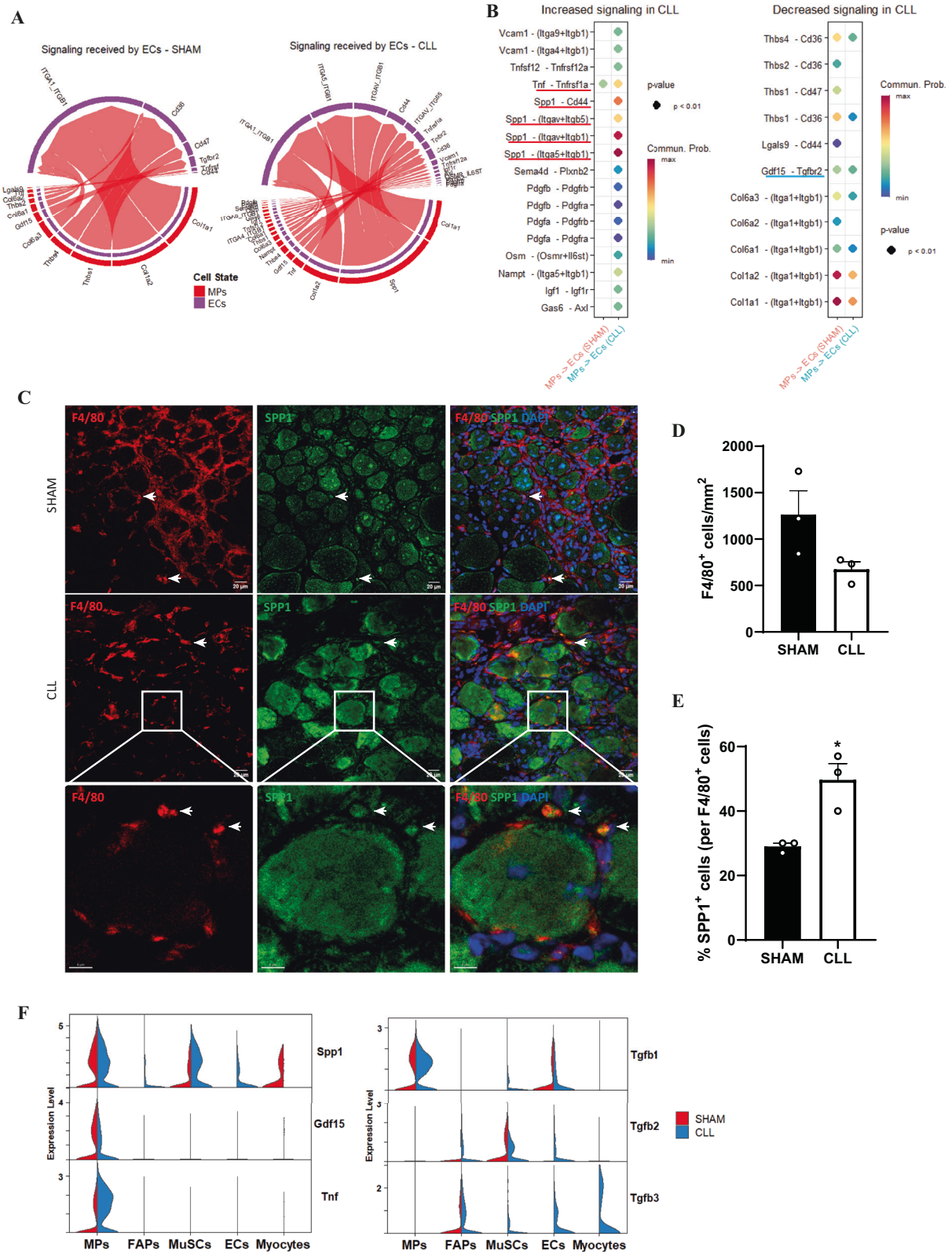

Vehicle vs OPNi, respectively, $P < 0.05$, Supplementary Fig. 7C), confirming an effective suppression of SPP1 signalling on MPs.

We next went on to assess how the lower expression of SPP1 affected the phenotypic fate of ECs. Immunostaining of muscle sections (Fig. 7A) revealed that inhibition of SPP1 was able to attenuate the onset of EndMT in CLL-treated mice. OPNi-treated animals exhibited an increased number of $CD31^+$ cells (364.4 ± 44.3 cells/mm^2 vs 593.5 ± 36 cells/mm^2, Vehicle vs OPNi respectively, $P < 0.05$, Fig. 7B) and a higher $CD31^+$ area when compared with vehicle-treated controls (33.7 ± 4.1 Vessels n/ROI vs 58.8 ± 7.4 Vessels n/ROI, Vehicle vs OPNi respectively, $P < 0.05$, Fig. 7B, Supplementary Fig. 7D). Consistently, vessel quantification analysis demonstrated a significant increase in total vessel area (2501.1 ± 263.8 μm^2/ROI vs

Fig. 5 | Analysis of MP-EC signalling interactions in regenerating muscle. **A** Chord diagram of MPs and ECs interactions. **B** Bubble plot showing all the significant interactions between MPs ligands and ECs receptors in both conditions. **C** Immunofluorescence staining of quadriceps muscle cross-sections of SHAM- and CLL-treated *Cdh5-CreER^{T2}:R26R-tdTomato* mice 5 days after CTX injection for MPs (F4/80, red), osteopontin (SPP1, green), and nuclear marker (DAPI, blue). White arrows indicate examples of Macrophages expressing SPP1. Magnification 40x, Scale bar at 20 µm and amplified images at 8 µm. **D** Quantification of F4/80^{+} cells per square millimetre in quadriceps muscle cross-sections of SHAM- and CLL-treated *Cdh5-CreER^{T2}:R26R-tdTomato* mice 5 days after CTX injection ($n = 3$, with three representative sections of each muscle examined). $P = 0.0940$ (two-tailed unpaired Student's *t*-test). **E** Frequency (in %) of SPP1^{+} macrophages from quadriceps muscle cross-sections of SHAM- and CLL-treated *Cdh5-CreER^{T2}:R26R-tdTomato* mice 5 days after CTX injection ($n = 3$, with three representative sections of each muscle examined). Statistically significant difference is indicated as ∗ representing $P < 0.05$ (two-tailed unpaired Student's *t*-test). **F** Violin Plot showing the expression of the different TGF-β isoforms, *Tnf*, *Gdf15* and *Spp1* on MPs, FAPs, MuSCs, ECs and myocyte populations between conditions.

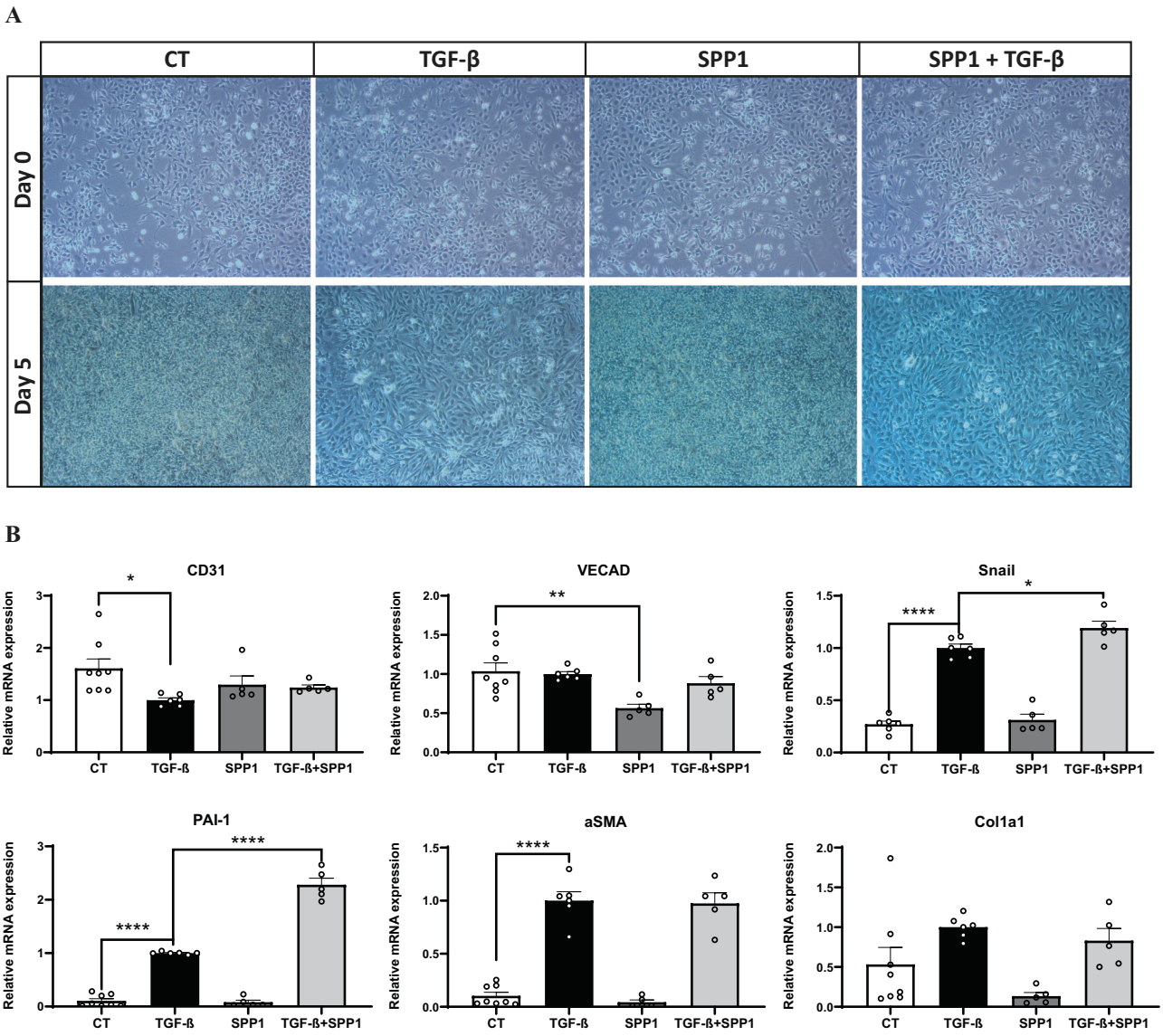

Fig. 6 | TGF-β and SPP1 synergize to induce EndMT in mouse skeletal muscle ECs. **A** mECs at day 0 and day 5, in the different experimental conditions: Control (CT), TGF-β, SPP1, SPP1 + TGF-β. **B** Relative gene expression levels of endothelial and mesenchymal markers of CT, TGF-β, SPP1, SPP1 + TGF-β treated mECs. Results are normalized to GAPDH. Data is presented as mean ± SEM ($n = 3$). Statistically significant differences are indicated as ∗, ∗∗, ∗∗∗ and ∗∗∗∗ representing $P < 0.05$, $P < 0.01$, $P < 0.001$ and $P < 0.0001$, respectively (two-tailed unpaired Student's *t*-test).

5020.2 ± 790.9 µm^2/ROI, Vehicle vs OPNi respectively, P < 0.05, Supplementary Fig. 7D), as well as a recovery of large vessels area (1250.6 ± 52.2 µm^2 vs 3234.7 ± 551.4 µm^2, Vehicle vs OPNi respectively, $P < 0.05$, Supplementary Fig. 7E). In parallel, SPP1 inhibition was associated with a reduction of ECs undergoing EndMT. This was evidenced by a decreased number of CD31^{+} cells co-expressing EC and mesenchymal markers, including tdTomato (178 ± 13 cells/mm^2 vs 91 ± 5 cells/mm^2, Vehicle vs OPNi respectively, $P < 0.01$, Fig. 7C), Col1a1 (58 ± 2 cells/mm^2 vs 30 ± 4 cells/mm^2, Vehicle vs OPNi respectively, $P < 0.01$, Fig. 7D), and tdTomato^{+}/Col1a1^{+} cells (147 ± 26 cells/mm^2 vs 67 ± 12 cells/mm^2, Vehicle vs OPNi respectively, $P < 0.05$, Fig. 7E), indicating a restoration of EC phenotypic identity.

Taken together, these findings indicate that although SPP1 does not significantly alter MP abundance during muscle regeneration, elevated

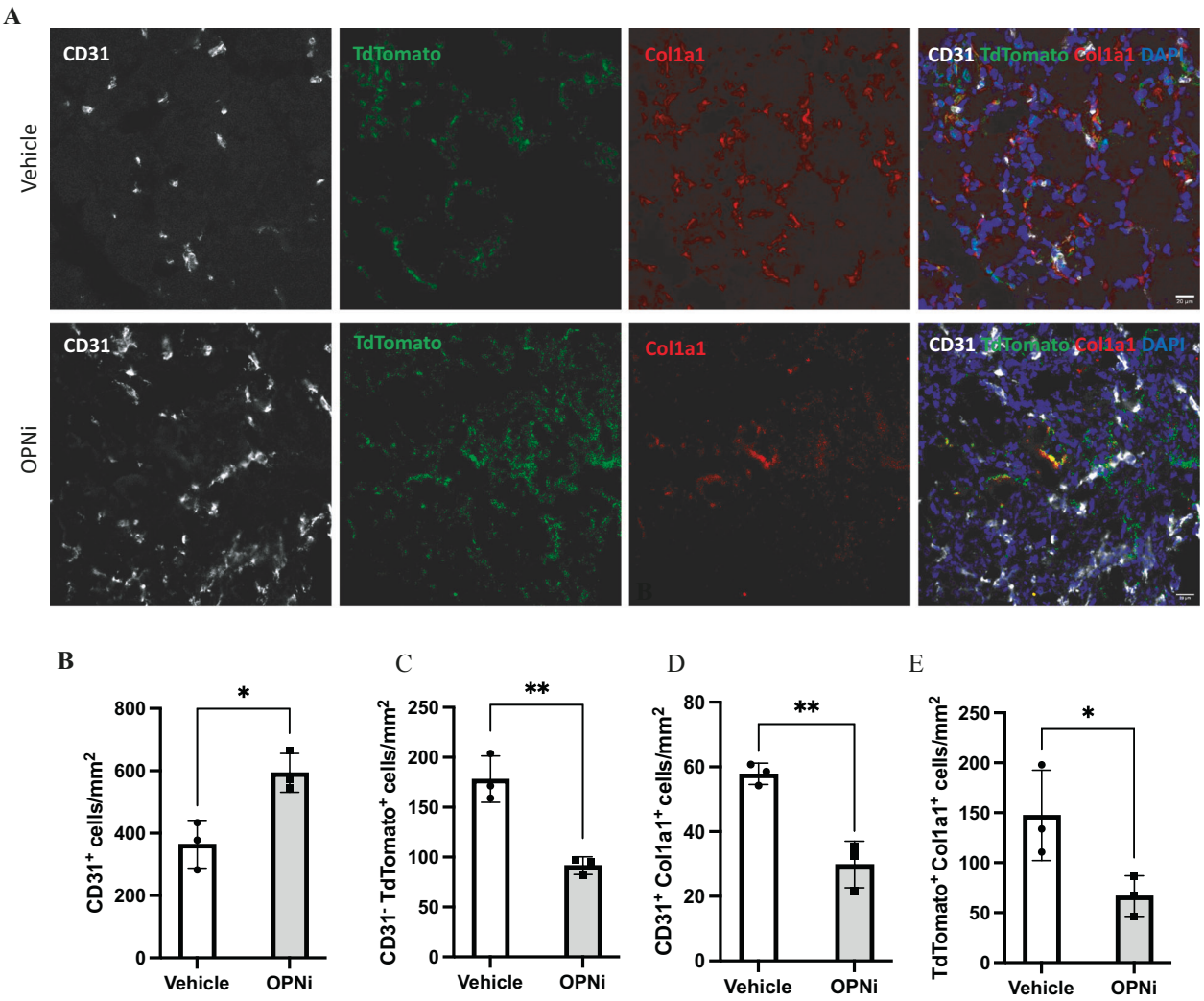

Fig. 7 | In vivo SPP1 inhibition attenuates EndMT in mouse skeletal muscle and restores ECs morphology. A Immunofluorescence staining of quadriceps muscle cross-sections of Vehicle- and OPNi-treated *Cdh5-CreER^{T2}:R26R-tdTomato* mice 5 days after CTX injection for ECs (CD31, white), tdTomato (green), Col1a1 (red) and nuclear marker (DAPI, blue). Magnification 40x, Scale bar at 20 µm. **B** Quantification of CD31$^+$ cells per square millimetre in quadriceps muscle cross-sections of Vehicle- and OPNi-treated *Cdh5-CreER^{T2}:R26R-tdTomato* mice 5 days after CTX injection ($n = 3$, with three representative sections of the muscle examined). Statistically significant differences are indicated as ∗ representing $P < 0.05$ (two-tailed unpaired Student's *t*-test). **C** Quantification of CD31$^-$tdTomato$^+$ cells per square millimetre in quadriceps muscle cross-sections of Vehicle- and OPNi-treated *Cdh5-CreERT2:R26R-tdTomato* mice 5 days after CTX injection ($n = 3$, with three representative sections of the muscle examined). Statistically significant differences are indicated as ∗∗ representing $P < 0.01$ (two-tailed unpaired Student's *t*-test). **D** Quantification of CD31$^+$Col1a1$^+$ cells per square millimetre in quadriceps muscle cross-sections of Vehicle- and OPNi-treated *Cdh5-CreERT2:R26R-tdTomato* mice 5 days after CTX injection ($n = 3$, with three representative sections of each muscle examined). Statistically significant differences are indicated as ∗∗ representing $P < 0.01$ (two-tailed unpaired Student's *t*-test). **E** Quantification of tdTomato$^+$Col1a1$^+$ cells per square millimetre in quadriceps muscle cross-sections of Vehicle- and OPNi-treated *Cdh5-CreER^{T2}:R26R-tdTomato* mice 5 days after CTX injection ($n = 3$, with three representative sections of each muscle examined). Statistically significant differences are indicated as ∗ representing P < 0.05 (two-tailed unpaired Student's *t*-test).

SPP1 expression promotes a shift of ECs toward a mesenchymal phenotype. This induction of EndMT impairs vascular remodelling and disrupts the proper establishment of a regenerative microenvironment. Thus, SPP1 emerges as a key mediator of MP-EC during muscle repair.

Discussion

Following muscle injury, sequential and coordinated events unfold to ensure effective muscle healing. During this process, inflammatory cells, particularly MPs, play a fundamental role by contributing to the phagocytosis of damaged tissue and by providing the necessary signals that support the activation and function of other cell types[2]. We have previously shown that infiltrating MPs restrict ECs phenotype and prevent the development of persistent tissue fibrosis during regeneration[8].

In this study, to gain a comprehensive understanding of MP influence on cell–cell interactions, we performed single-cell RNA sequencing of the regenerating skeletal muscle 5 days post-CTX injury under conditions of partially impaired MP recruitment. We found that disrupted MP recruitment dynamics resulted in marked alterations in the cellular composition of the regenerating niche. As expected, MPs were significantly reduced in the CLL condition compared to SHAM controls. Even though other immune populations—including dendritic cells and immune myeloid subsets—also showed a decrease, this reduction was quantitatively less pronounced than that observed for MPs. An important methodological consideration is that CLL liposomes preferentially target actively phagocytic circulating and infiltrating MPs. While resident macrophage populations may also contribute to niche regulation, the present study focuses on the consequences of altered recruitment dynamics and does not specifically dissect the relative

contribution of resident versus monocyte-derived macrophage subsets. Nonetheless, MPs represent the predominant immune compartment in regenerating muscle and exhibit the most pronounced quantitative reduction following CLL treatment, whereas adaptive immune populations are largely preserved. Additionally, mesenchymal populations, particularly FAPs, were markedly expanded following CLL treatment, whereas ECs were substantially reduced. These compositional shifts correlate with the histological differences observed between conditions and support the notion that selective impairment of MP recruitment profoundly reshapes the regenerative microenvironment rather than only inducing a uniform suppression of all immune compartments. In this context, ECs undergo a transition toward a mesenchymal phenotype, compromising angiogenesis, disrupting crosstalk with immune and myogenic compartments, and promoting extracellular matrix deposition. Simultaneously, the reduced MP population in regenerating muscle displays an altered phenotypic profile, with M2-like MPs exhibiting activation of pro-inflammatory programs, including enhanced glycolytic metabolism, HIF-1α, and TNF signalling, while suppressing pro-regenerative and pro-angiogenic functions. These findings suggest that adequate MP recruitment is required to support proper MP polarization and to maintain a balanced inflammatory environment conducive to EC stability. Consistently, intercellular communication analysis and immunostaining identified specific ligand–receptor interactions between MPs and ECs—most prominently involving SPP1. In vivo studies further support the existence of crosstalk between MPs and ECs that is dependent on SPP1, as its inhibition ameliorated the previously observed dysfunctional features and reduced the induction of EndMT, highlighting a complex SPP1-dependent signalling network that modulates EC behaviour.

The essential role of monocyte-derived MPs in skeletal muscle regeneration has been demonstrated through myeloid-cell depletion studies[8,44,45] and MP recruitment blockade via MCP-1/CCR2 receptor knockout models[46,47]. In these animals, a significant impairment in muscle regeneration is observed, characterized by delayed myogenesis and angiogenesis, excessive ECM deposition, and increased adipocyte populations[8,44–47]. The balance between pro- and anti-inflammatory/ pro-regenerative MPs, alongside their transition from a TNF-rich to a TGF-β1-rich microenvironment, has been identified as critical for proper muscle healing[4,45] and FAPs dynamics[7]. In dystrophic muscle environments, where the MP phenotypic switch is disrupted, a large subset of MPs simultaneously expresses TNF and TGF-β1, leading to a breakdown of the ordered inflammatory transition, triggering FAPs survival and muscle fibrosis[7]. Consistent with this, we observed a correlation between higher FAP numbers and impaired MP inflammatory profiles. In addition, increased FAP abundance was associated with suppression of Notch and Hedgehog signalling and dysregulated metabolic profile, specifically anabolic metabolism activation. While the MP inflammatory transition is known to control FAP dynamics, we provide evidence that this proper polarization is also key for restricting EC phenotype and function during regeneration. Indeed, the correct expansion of $CD206^{+}$ MPs has been shown to be essential to prevent EndMT in the muscle[10].

The involvement of EndMT and the influence of TGF-β signalling in the pathogenesis of fibrotic diseases have been well documented[25–27,48]. In line with this, our findings revealed TGF-β signalling activation in ECs undergoing EndMT during impaired skeletal muscle regeneration. Elevated TGF-β levels in muscle, five days post-injury, has been previously reported where impaired MP recruitment was associated with increased EndMT[8]. While MPs do not appear to be the primary source of TGF-β at this stage, the observed upregulation of TGF-β2 and TGF-β3 in FAPs, MuSCs, myocytes, and ECs in CLL-treated mice likely contributes to increased TGF-β levels in muscle. Therefore, these increased TGF-β levels, together with higher MP-derived TNF expression drive the disruption of the inflammatory environment and commit ECs to a mesenchymal fate. Our results additionally demonstrate that the onset of EndMT adversely impacts ECs function. Specifically, we observed reductions in ECs population, alterations in their distribution, morphology, and transcriptional signature patterns. These changes ultimately affect blood vessel formation and growth, as corroborated by the visualization of Hippo signalling activation and simultaneous suppression of the Notch pathway.

The onset of EndMT in our model is coupled with deregulation of other cross-signalling events, prominently involving SPP1. SPP1 is an inflammatory cytokine that is minimally expressed under homoeostatic conditions but becomes strongly upregulated by MPs and myogenic cells following injury[49,50]. Although SPP1 does not directly contribute to the structural integrity of the ECM, its capacity to bind multiple ECM components allows it to modulate matrix organization and cellular interactions. In skeletal muscle, SPP1 supports neutrophil and MP infiltration and contributes to tissue repair[50]. However, aberrant or sustained SPP1 expression has been associated with pathological inflammation and fibrosis in several tissues[51,52], where it regulates MP–FAP interactions and influences FAP differentiation[25,42].

In our study, we demonstrate that SPP1 cooperates with TGF-β to promote EndMT in vitro, supporting a synergistic model of ECs phenotypic transition. Importantly, in vivo pharmacological inhibition of SPP1 in CLL-treated mice attenuated EndMT-associated features, partially restoring ECs identity and improving vascular architecture. These findings indicate that while SPP1 alone may not be sufficient to induce EndMT, it plays a significant contributory role in amplifying endothelial dysfunction within an inflammatory and pro-fibrotic niche. Consistently, inhibition of the TGF-β pathway has been shown to reduce fibrosis and EndMT in multiple pathological contexts, including vascular remodeling and muscular dystrophy models[53–55]. Together, these observations reinforce the concept that SPP1 operates within a broader TGF-β–dependent signalling axis that drives endothelial phenotypic instability under inflammatory conditions.

The interplay between SPP1, TGF-β, and TNF signalling is supported by previous studies showing that TNF enhances TGF-β–induced EndMT[33]. In dystrophic muscle, SPP1 contributes to TGF-β processing in fibroblasts and skews MP polarization toward a pro-inflammatory phenotype[38,56]. Moreover, recent single-cell RNA sequencing analyses in Duchenne Muscular Dystrophy (DMD) muscles identified a subset of capillary ECs expressing collagen-related genes and fibronectin. These alterations were attributed to stromal and MP-derived factors, including TGF-β, SPP1, TNF-α, and IL-1β, which activate TGF-β signaling in ECs and promote endothelial dysregulation[57]. Our findings are consistent with this inflammatory signalling axis and further support the concept that MP-derived cues reshape endothelial fate during pathological muscle remodeling.

Beyond their established role in angiogenesis, ECs actively contribute to the regulation of the regenerating muscle niche. Loss of endothelial identity has been associated with impaired coordination between angiogenesis and myogenesis, as observed in dystrophic conditions where ECs co-express mesenchymal markers and display altered extracellular matrix organization[11,57]. Effective regeneration requires tight temporal coordination between vascular remodeling and muscle stem cell (MuSC) activation, a process supported by properly polarized MPs[31]. In our model, immune dysregulation and enhanced EndMT were accompanied by alterations in endothelial signalling pathways implicated in niche homeostasis, suggesting that endothelial instability may have broader consequences for regenerative coordination. However, the precise downstream effects of EndMT on muscle stem cell dynamics remain to be fully elucidated.

Collectively, our data support a model in which temporally coordinated integration of inflammatory, angiogenic, and myogenic signals is essential for effective skeletal muscle regeneration. Proper MP recruitment and polarization, together with tightly regulated cytokine expression—including TGF-β, TNF, and SPP1—are critical for preserving endothelial identity and preventing EndMT. Targeting this inflammatory–endothelial axis may represent a promising therapeutic approach in muscular dystrophy and age-associated regenerative decline.

Materials and methods

Mice

The mouse strains used in this study have been previously described[58,59]. All transgenic mouse lines were maintained on a CD45.2 C57BL/6 genetic

background. A specific lineage tracing mouse model - *Cdh5-CreER^{T2}:R26R-tdTomato* – was employed for the in vivo studies on EndMT. Homozygous transgenic mice expressing a tamoxifen (TAM)-inducible form of Cre recombinase (*CRE-ER^{T2}*) under the control of the endothelial-specific gene VE-Cadherin (*Cdh5*)[59] were crossed with *R26R-tdTomato* homozygous reporter mice (The Jackson Laboratory - RRID:IMSR_JAX:007909). Cre recombination was then induced in double transgenic mice at postnatal days 6-7-8 with three subcutaneous (SC) injections of 25 µl TAM at 10 mg/ml (Sigma-Aldrich, St. Louis). Mice were kept under controlled conditions (12 h light/dark cycle and room temperature at 22 °C) and had free access to tap water and standard mice chow. Mice were randomly assigned to experimental groups (at least 3 animal/group/timepoint). Our study examined male and female animals, and similar findings are reported for both sexes

All animal procedures were performed at San Raffaele Scientific Institute animal facilities in accordance with European Union guidelines and with the approval of the Institutional Ethical Committee and Ministry of Health (Authorizations 244/2020-PR, 101/2023-PR, 575/2024-PR).

We have complied with all relevant ethical regulations for animal use.

Muscle injury

For muscle injury experiments, 8-9 weeks-old mice were anesthetized with isoflurane and quadriceps muscle was injected with cardiotoxin (CTX) (Latoxan) at 10 µM (100 µl per muscle) to induce muscle injury followed by regeneration. Muscles were then collected and processed for analysis 5 days after. For histology and immunofluorescence studies, muscles were collected and directly frozen in isopentane cooled in liquid nitrogen and stored at -80 °C.

Depletion of circulating monocytes

8-9 weeks-old *Cdh5-CreER^{T2}:R26R-tdTomato* mice were intravenously injected (tail veins) with 200 µl liposomes containing Clodronate (CLL) - to deplete peripheral blood circulating monocytes and compromise macrophage recruitment to the site of injury - or 200 µl PBS liposomes as control (SHAM). CLL and SHAM injections were performed one day before and two days after acute damage induction by CTX on quadriceps. CLL and SHAM liposomes were purchased from: http://www.clodronateliposomes.org/ashwindigital.asp?docid=26.

To confirm an effective reduction of circulating monocytes in CLL vs SHAM-treated mice, blood was collected 4 days after CTX injection and processed for FACS analysis. Briefly, samples were stained and analysed in CMF (Calcium/Magnesium-Free PBS, 10% FBS, 5% Pen/Strep, 2 mM EDTA), incubated for 15 min with 0.5 mg/mL Fc block (1:500) (BD Biosciences, Franklin Lakes, NJ, USA) and labelled with a combination of PE-conjugated rat anti-CD45 (1:400) (BD Biosciences), PE-Cy7-conjugated rat anti-CD11b (1:200) (BD Biosciences) and APC-conjugated rat anti-F4/80 (1:200) (BD Biosciences). Appropriate fluorescence gating parameters were established with compensation beads (BD Biosciences), unstained, and fluorescence-minus-one (FMO) staining. In all samples, doublets were gated out using pulse geometry gates (FSC-H versus FSC-A and SSC-H versus SSC-A), whereas dead cells were excluded using Hoechst 33258 (Hellobio, Bristol, UK). Suspensions were analyzed using a Fortessa X-20 analyzer (BD Biosciences) and FlowJo software v10 (FlowJo/BD, Ashland, OR, USA).

Cell isolation from skeletal muscle

In brief, freshly isolated quadriceps were minced into small pieces and enzymatically dissociated with 1.5 mg/mL Dispase (Gibco, 17105-041) and 0.12% (w/v) Collagenase type I (Sigma-Aldrich, C0130) in two cycles of 30 min at 37 °C under constant 240 rpm agitation. The suspension was then passed through a 16 G needle, followed by a 26 G needle, and filtered through a 40 µm sterile strainer. Then cold CMF was added to inactivate enzymes and red blood cells lysed. To remove cell debris from the suspensions, Ficoll separation was performed. Cells were resuspended in 7 mL of pre-warmed DMEM High Glucose (Gibco, 41965-039) supplemented with 10% FBS (Gibco, 10270-106), in a 15 mL falcon, and 3.5 mL of Ficoll was slowly layered on top. Samples were centrifuged at 300 *g* for 30 minutes with no brake or acceleration and the cell layer formed aspirated to another falcon and washed with cell medium.

scRNA-seq

After obtaining a clean single-cell suspension, samples were processed on the 10x Chromium Genomics platform using the Chromium Single Cell 3′ Library & Gel Bead Kit v3 kit (10×). After quality controls and quantification on the TapeStation instrument (Agilent), libraries were sequenced on NextSeq500 platforms (Illumina), generating around 100,000 reads/cell. Raw sequencing data was demultiplexed with the mkfastq application (Cell Ranger v.3.0.2). Reads were aligned to the reference genome and assigned to genes with cellranger count (Cell Ranger v.3.0.2, genome: refdata-gex-mm10-2020-A), with the expect-cells option set to 10,000. The produced filtered matrices were used for further bioinformatic analysis on R.

scRNA-seq data analysis

Seurat 4.3.0.1[60] was used to analyse scRNA-seq data. All samples were filtered for quality control parameters (cells with more than 8% reads mapping to mitochondrial genes, feature counts greater than 7000 and smaller 350 and cells with less than 1000 transcripts were filtered out) and DoubletFinder[61] function was performed. Applying these filters eliminated dying cells and doublets. Data was then normalized, scaled, and dimensionality reduction performed through Principal Component Analysis (PCA) following Seurat's tutorial as evaluated by elbow plots. Cells from all samples were combined and batch correction was executed using Harmony[62] (version 1.1), and unsupervised clustering was performed. UMAP embedding parameters were based on the top 75 PCs and 0.9 dimensions for visualization. Each cluster was labelled based on canonical skeletal muscle gene expression. Differential expression analysis between conditions was conducted using DESeq2 (version 1.44.0). For each comparison, log2 (fold change) results were shrunken using the apeglm[63] package (version 1.26.1) to remove noise (differentially expressed genes with low counts and/or high dispersion values) while preserving significant differences.

Gene Set Enrichment Analysis (GSEA)

Gene Set Enrichment analysis (GSEA) was conducted using differentially expressed genes (DEG) evaluated by the DEseq2 package. All genes were ranked according to the log2FoldChange and GSEA analysis carried out using R package ClusterProfiler[64] (version 4.12.6), querying the Gene Ontology (GO) and KEGG database. The analysis was performed by setting the minimum gene set to 10 and maximum to 800. GO and KEGG terms were considered significant with a selected cutoff p-value of 0.05.

Immunofluorescence

Serial 10 µm thick muscle sections were sectioned on a cryostat (Leica CM 3050S), collected on Superfrost microslides (VWR) and stored at -80 °C until analysis. For immunofluorescence muscle cryosections were thawed and fixed with 4% PFA in PBS for 10 minutes. Slides were then washed with PBS and permeabilized with 0.2% Triton and 1% BSA solution in PBS for 30 min, at RT. After, slides were blocked in 10% Donkey serum (DS) and 1% BSA solution in PBS, for 30 min, and then incubated with primary antibodies (Table 1) in 1% DS in PBS overnight, in a wet chamber, at 4 °C. The following day, slides were washed in PBS and incubated with secondary antibodies (Table 1) in 1% DS in PBS for 1 hour at RT. Then, they were washed again, counterstained and mounted (Fluoroshield™ with 4',6-diamidino-2-phenyl-indole (DAPI), Sigma-Aldrich, F6057). Slides were examined and images were acquired using a Zeiss 710 confocal microsope equipped with an EC Plan-Neofluar 40x/1.30 Oil DIC M27. A minimum of 3 animals per group was used and at least 3 different fields per animal acquired. Counts from all fields corresponding to one animal were averaged. For quantification of cell numbers per field, individual cells were

Table 1 | List of antibodies and concentrations

Antibody			Concentration
RFP	Rabbit	600-401-379 Rockland	1:400
RFP	Chicken	600-901-379 Rockland	1:100
CD31	Goat α-mouse	AF3628 R&D Systems	1:200
F4/80	Rat α-mouse	MCA497 Bio-Rad	1:100
Col1a1	Rabbit α-mouse	PA529569 Invitrogen	1:200
SPP1	Rabbit α-mouse	PA5-141129 Invitrogen	1:100
PDGFRα	Rat α-mouse	MAB3221 R&D Systems	1:100
Alexa Fluor 568	Donkey α-rat	A78946 Invitrogen	1:500
Alexa Fluor 488	Donkey α-chicken	A78948 Invitrogen	1:500
Alexa Fluor 488	Donkey α-rabbit	A32790 Invitrogen	1:500
Alexa Fluor 555	Donkey α-rabbit	A32794 Invitrogen	1:500
Alexa Fluor 647	Donkey α-goat	A32849 Invitrogen	1:500
Alexa Fluor 555	Donkey α-goat	A32816 Invitrogen	1:500

Table 2 | List of primer sequences

Primer		Sequence
GAPDH	Fwd	5' AACTTTGGCATTGTGGAAGG 3'
	Rev	5' ACACATTGGGGGTAGGAACA 3'
CD31	Fwd	5′-AGGGGACCAGCTGCACATTAGG-3′
	Rev	5′-AGGCCGCTTCTCTTGACCACTT-3′
VE-CAD	Fwd	5′-GTACAGCATCATGCAGGGCG-3′
	Rev	5′-ATTCGTATCGGATAGTGGGG-3′
αSMA	Fwd	5′-TCACCATTGGAAACGAACG-3′
	Rev	5′-ATAGGTGGTTTCGTGGATGC-3′
SNAIL1	Fwd	5′-CCACTGCAACCGTGCTTTT-3′
	Rev	5′-ATGTCCTTGCTCCACAAGCAC-3′
Col1a1	Fwd	5′-GGTATGCTTGATCTGTATCTGC-3′
	Rev	5′-AGTCCAGTTCTTCATTGCATT-3′
PAI-1	Fwd	5′-TCCTCCACAGCCTTTGTCAT-3′
	Rev	5′-ACATCTCCACTTTCGTCCCA-3′

manually counted using the appropriate channels in combination with DAPI to identify nuclei on the software Fiji/ImageJ.

Vessel density and morphology analysis

Vessel density and morphology were quantified on muscle cross-sections using immunofluorescence confocal microscopy by analyzing the CD31-positive signal. Image analysis was performed using Fiji software. $CD31^+$ structures were identified by applying a threshold-based binary mask, and particle analysis included only objects with an area > 8.8 μm².

For each particle, the following parameters were measured: number, area, roundness index, and aspect ratio. Vessel cross-sections were subsequently classified into morphological subsets based on these shape descriptors, as shown in Fig. S3.

Particle roundness was assessed using two shape descriptor parameters: the roundness index (RI), defined as $4 \times \text{Area} / (\pi \times \text{major axis}^2)$, and the aspect ratio (AR), defined as the ratio of the major axis to the minor axis of the best-fitting ellipse. In our analysis, round vessels were defined as particles with RI > 0.5 and AR < 2. Large vessels were defined as particles with an area > 100 μm².

Cell culture

Mouse ECs previously isolated from skeletal muscle[43] were seeded at a density of 3125 cells/cm², in 6-well culture plates (ThermoFisher Scientific, USA) coated with 0.1% Gelatin (Merck, G1393). Cells were cultured in DMEM High Glucose (Gibco, 41965-039) supplemented with 10% FBS (Gibco, 10270-106), 1% Pen Strep (Gibco, 15140-122), 1% L- Glutamine (Gibco, 25030-024) and 10 ng/mL of VEGF (Cell Signalling, 5211SF) for 24 h. After this, mECs were switched to starvation (2% FBS) for another 24 h. At the end of this period, mECs were cultured in the same starvation medium with or without 10 ng/mL of TGF-β1 (Cell Signalling, 5231LC), 100 or 200 ng/mL of SPP1 (R&D Systems, 441-OP-050), or 500 ng/mL of GDF-15 (R&D Systems, 8944-GD-025) for 3 and 5 days. Then, cells were collected, and gene expression assessed by rt-qPCR analysis.

RNA extraction and cDNA synthesis

Total RNA from mECs was isolated using ReliaPrep RNA Cell Miniprep System (Z6011; Promega, Milan, Italy), following manufacturer instructions. Total RNA was quantified by measuring the absorbance at 260 nm in a Nanodrop (Thermofisher Scientific) and RNA purity was evaluated by the ratio of absorbance at 260 and 280 nm. RNA samples were reverse transcribed to cDNA with the LunaScript RT SuperMix Kit (E3010L) from New England Biolabs, using the Thermocycler 2027 (Applied Biosystems).

Real-time rt-qPCR analysis

Real-time rt-qPCR was carried out using the Luna Universal qPCR Master Mix (M3003X, New England Biolabs) and specific primers (Table 2) in a QuantStudio™ 7 Flex Real-Time PCR System (Applied Biosystems). Amplification reactions were performed in duplicate. To check specificity, a dissociation curve was derived at the end of each run. Controls lacking reverse transcriptase were included to ensure no genomic DNA contamination during preparations. Results were normalized to GAPDH expression.

In vivo inhibition of SPP1

To achieve inhibition of SPP1, 8–9-week-old *Cdh5-CreER^{T2}:R26R-tdTomato* mice were intravenously injected with 200 μl of clodronate-containing liposomes (CLL), as previously described. Muscle injury was induced in the quadriceps by CTX injection. Mice were then randomly assigned into two groups: three mice received 5 mg/kg of the OPN expression inhibitor 1 (OPN-IN-1) (HY-146064, MedChemExpress) by intraperitoneal injection on the day of muscle injury and three days later, while control mice received an equivalent volume of vehicle as in refs. 65,66. Animals were euthanized 5 days after CTX injection, and quadriceps muscles were collected for immunofluorescence staining.

Statistical analysis

Differences between the two experimental groups were compared by Student's t-test using GraphPad Prism 8. Statistical significance was accepted for comparisons where $p < 0.05$. Values are presented as means ± S.E.M.

Reporting summary

Further information on research design is available in the Nature Portfolio Reporting Summary linked to this article.

Data availability

The single-cell RNA sequencing data generated in this study have been deposited in the GEO database under accession code GSE291782 and are available at the following URL: https://www.ncbi.nlm.nih.gov/geo/query/acc.cgi?acc=GSE291782. All other data supporting the findings of this study are available within the paper and its Supplementary Information.

Received: 23 March 2025; Accepted: 23 April 2026;
Published online: 11 May 2026

References

1. Varga, T. et al. Tissue LyC6- macrophages are generated in the absence of circulating LyC6- monocytes and Nur77 in a model of muscle regeneration. *J. Immunol.* **191**, 5695–5701 (2013).
2. Chazaud, B. Inflammation and skeletal muscle regeneration: leave it to the macrophages!. *Trends Immunol.* **41**, 481–492 (2020).
3. Wosczyna, M. N. et al. Mesenchymal stromal cells are required for regeneration and homeostatic maintenance of skeletal muscle. *Cell Rep.* **27**, 2029–2035.e2025 (2019).
4. Saclier, M. et al. Differentially activated macrophages orchestrate myogenic precursor cell fate during human skeletal muscle regeneration. *Stem Cells* **31**, 384–396 (2013).
5. Varga, T. et al. Highly dynamic transcriptional signature of distinct macrophage subsets during sterile inflammation, resolution, and tissue repair. *J. Immunol.* **196**, 4771–4782 (2016).
6. Juban, G. & Chazaud, B. Metabolic regulation of macrophages during tissue repair: insights from skeletal muscle regeneration. *FEBS Lett.* **591**, 3007–3021 (2017).
7. Lemos, D. R. et al. Nilotinib reduces muscle fibrosis in chronic muscle injury by promoting TNF-mediated apoptosis of fibro/adipogenic progenitors. *Nat. Med.* **21**, 786–794 (2015).
8. Zordan, P. et al. Macrophages commit postnatal endothelium-derived progenitors to angiogenesis and restrict endothelial to mesenchymal transition during muscle regeneration. *Cell Death Dis.* **5**, e1031 (2014).
9. Uezumi, A. et al. Identification and characterization of PDGFRα+ mesenchymal progenitors in human skeletal muscle. *Cell Death Dis.* **5**, e1186 (2014).
10. Iavarone, F. et al. Cripto shapes macrophage plasticity and restricts EndMT in injured and diseased skeletal muscle. *EMBO Rep.* **21**, e49075 (2020).
11. Pessina, P. et al. Fibrogenic cell plasticity blunts tissue regeneration and aggravates muscular dystrophy. *Stem Cell Rep.* **4**, 1046–1060 (2015).
12. De Micheli, A. J. et al. Single-cell analysis of the muscle stem cell hierarchy identifies heterotypic communication signals involved in skeletal muscle regeneration. *Cell Rep.* **30**, 3583–3595.e3585 (2020).
13. Oprescu, S. N., Yue, F., Qiu, J., Brito, L. F. & Kuang, S. Temporal dynamics and heterogeneity of cell populations during skeletal muscle regeneration. *iScience* **23**, 100993 (2020).
14. Murphy, A. E. & Skene, N. G. A balanced measure shows superior performance of pseudobulk methods in single-cell RNA-sequencing analysis. *Nat. Commun.* **13**, 7851 (2022).
15. Squair, J. W. et al. Confronting false discoveries in single-cell differential expression. *Nat. Commun.* **12**, 5692 (2021).
16. Farup, J. et al. Human skeletal muscle CD90(+) fibro-adipogenic progenitors are associated with muscle degeneration in type 2 diabetic patients. *Cell Metab.* **33**, 2201–2214.e2211 (2021).
17. Reggio, A. et al. Metabolic reprogramming of fibro/adipogenic progenitors facilitates muscle regeneration. *Life Sci. Alliance* **3**, e202000646 (2020).
18. Kopinke, D., Roberson, E. C. & Reiter, J. F. Ciliary Hedgehog Signaling Restricts Injury-Induced Adipogenesis. *Cell* **170**, 340–351.e312 (2017).
19. Marinkovic, M. et al. Fibro-adipogenic progenitors of dystrophic mice are insensitive to NOTCH regulation of adipogenesis. *Life Sci. Alliance* **2**, e201900437 (2019).
20. Feng, Y. et al. YAP promotes ocular neovascularization by modifying PFKFB3-driven endothelial glycolysis. *Angiogenesis* **24**, 489–504 (2021).
21. Kim, J. et al. YAP/TAZ regulates sprouting angiogenesis and vascular barrier maturation. *J. Clin. Invest.* **127**, 3441–3461 (2017).
22. Wang, X. et al. YAP/TAZ Orchestrate VEGF Signaling during Developmental Angiogenesis. *Dev. Cell* **42**, 462–478.e467 (2017).
23. Blanco, R. & Gerhardt, H. VEGF and Notch in tip and stalk cell selection. *Cold Spring Harb. Perspect. Med.* **3**, a006569 (2013).
24. Mack, J. J. et al. NOTCH1 is a mechanosensor in adult arteries. *Nat. Commun.* **8**, 1620 (2017).
25. Cooley, B. C. et al. TGF-β Signaling Mediates Endothelial-to-Mesenchymal Transition (EndMT) during vein graft remodeling. *Sci. Transl. Med.* **6**, 227ra234–227ra234 (2014).
26. Hashimoto, N. et al. Endothelial-mesenchymal transition in bleomycin-induced pulmonary fibrosis. *Am. J. Respir. Cell Mol. Biol.* **43**, 161–172 (2010).
27. Zeisberg, E. M. et al. Endothelial-to-mesenchymal transition contributes to cardiac fibrosis. *Nat. Med* **13**, 952–961 (2007).
28. Kawasaki, K. et al. Activation of the Phosphatidylinositol 3-Kinase/Protein Kinase Akt Pathway Mediates Nitric Oxide-Induced Endothelial Cell Migration and Angiogenesis. *Mol. Cell. Biol.* **23**, 5726–5737 (2003).
29. Zhang, Z. et al. Activated phosphatidylinositol 3-kinase/Akt inhibits the transition of endothelial progenitor cells to mesenchymal cells by regulating the forkhead box subgroup O-3a signaling. *Cell Physiol. Biochem.* **35**, 1643–1653 (2015).
30. Christov, C. et al. Muscle satellite cells and endothelial cells: close neighbors and privileged partners. *Mol. Biol. Cell* **18**, 1397–1409 (2007).
31. Latroche, C. et al. Coupling between myogenesis and angiogenesis during skeletal muscle regeneration is stimulated by restorative macrophages. *Stem Cell Rep.* **9**, 2018–2033 (2017).
32. Lee, U. et al. A Tead1-Apelin axis directs paracrine communication from myogenic to endothelial cells in skeletal muscle. *iScience* **25**, 104589 (2022).
33. Coulis, G. et al. Single-cell and spatial transcriptomics identify a macrophage population associated with skeletal muscle fibrosis. *Sci. Adv.* **9**, eadd9984 (2023).
34. Patsalos, A. et al. Spatiotemporal transcriptomic mapping of regenerative inflammation in skeletal muscle reveals a dynamic multilayered tissue architecture. *J. Clin. Invest.* **134** (2024).
35. Sousa, N. S. et al. The immune landscape of murine skeletal muscle regeneration and aging. *Cell Rep.* **43**, 114975 (2024).
36. Arnold, L. et al. Inflammatory monocytes recruited after skeletal muscle injury switch into antiinflammatory macrophages to support myogenesis. *J. Exp. Med.* **204**, 1057–1069 (2007).
37. Tonkin, J. et al. Monocyte/Macrophage-derived IGF-1 orchestrates murine skeletal muscle regeneration and modulates autocrine polarization. *Mol. Ther.* **23**, 1189–1200 (2015).
38. Kramerova, I. et al. Spp1 (osteopontin) promotes TGFβ processing in fibroblasts of dystrophin-deficient muscles through matrix metalloproteinases. *Hum. Mol. Genet.* **28**, 3431–3442 (2019).
39. Yoshimatsu, Y. et al. TGF-beta and TNF-alpha cooperatively induce mesenchymal transition of lymphatic endothelial cells via activation of Activin signals. *PLOS ONE* **15**, e0232356 (2020).
40. Yoshimatsu, Y. et al. TNF-α enhances TGF-β-induced endothelial-to-mesenchymal transition via TGF-β signal augmentation. *Cancer Sci.* **111**, 2385–2399 (2020).
41. Patsalos, A. et al. A growth factor-expressing macrophage subpopulation orchestrates regenerative inflammation via GDF-15. *J Exp Med* **219** (2022).
42. Vetrone, S. A. et al. Osteopontin promotes fibrosis in dystrophic mouse muscle by modulating immune cell subsets and intramuscular TGF-beta. *J. Clin. Invest.* **119**, 1583–1594 (2009).
43. Ieronimakis, N., Balasundaram, G. & Reyes, M. Direct isolation, culture and transplant of mouse skeletal muscle derived endothelial cells with angiogenic potential. *PLoS One* **3**, e0001753 (2008).
44. Summan, M. et al. Macrophages and skeletal muscle regeneration: a clodronate-containing liposome depletion study. *Am. J. Physiol.-Regul. Integr. Comp. Physiol.* **290**, R1488–R1495 (2006).
45. Wang, H. et al. Altered macrophage phenotype transition impairs skeletal muscle regeneration. *Am. J. Pathol.* **184**, 1167–1184 (2014).

46. Martinez, C. O. et al. Regulation of skeletal muscle regeneration by CCR2-activating chemokines is directly related to macrophage recruitment. *Am. J. Physiol.-Regul. Integr. Comp. Physiol.* **299**, R832–R842 (2010).
47. Ochoa, O. et al. Delayed angiogenesis and VEGF production in CCR2−/− mice during impaired skeletal muscle regeneration. *Am. J. Physiol.-Regul. Integr. Comp. Physiol.* **293**, R651–R661 (2007).
48. Pardali, E., Sanchez-Duffhues, G., Gomez-Puerto, M. C. & Ten Dijke, P. TGF-β-induced endothelial-mesenchymal transition in fibrotic diseases. *Int. J. Mol. Sci.* **18** (2017).
49. Hirata, A. et al. Expression profiling of cytokines and related genes in regenerating skeletal muscle after cardiotoxin injection: a role for osteopontin. *Am. J. Pathol.* **163**, 203–215 (2003).
50. Wasgewatte Wijesinghe, D. K., Mackie, E. J. & Pagel, C. N. Normal inflammation and regeneration of muscle following injury require osteopontin from both muscle and non-muscle cells. *Skelet. Muscle* **9**, 6 (2019).
51. Freiholtz, D. et al. SPP1/osteopontin: a driver of fibrosis and inflammation in degenerative ascending aortic aneurysm? *J. Mol. Med.* **101**, 1323–1333 (2023).
52. Oh, K., Seo, M. W., Kim, Y. W. & Lee, D. S. Osteopontin potentiates pulmonary inflammation and fibrosis by modulating IL-17/IFN-γ-secreting T-cell ratios in bleomycin-treated mice. *Immune Netw.* **15**, 142–149 (2015).
53. Wang, X. & Zhou, L. The multifaceted role of macrophages in homeostatic and injured skeletal muscle. *Front. Immunol.* **14**, 1274816 (2023).
54. Stepien, D. M. et al. Tuning macrophage phenotype to mitigate skeletal muscle fibrosis. *J. Immunol.* **204**, 2203–2215 (2020).
55. Acuna, M. J. et al. Restoration of muscle strength in dystrophic muscle by angiotensin-1-7 through inhibition of TGF-beta signalling. *Hum. Mol. Genet.* **23**, 1237–1249 (2014).
56. Capote, J. et al. Osteopontin ablation ameliorates muscular dystrophy by shifting macrophages to a pro-regenerative phenotype. *J. Cell Biol.* **213**, 275–288 (2016).
57. Saleh, K. K. et al. Single cell sequencing maps skeletal muscle cellular diversity as disease severity increases in dystrophic mouse models. *iScience* **25**, 105415 (2022).
58. Madisen, L. et al. A robust and high-throughput Cre reporting and characterization system for the whole mouse brain. *Nat. Neurosci.* **13**, 133–140 (2010).
59. Wang, Y. et al. Ephrin-B2 controls VEGF-induced angiogenesis and lymphangiogenesis. *Nature* **465**, 483–486 (2010).
60. Hao, Y. et al. Integrated analysis of multimodal single-cell data. *Cell* **184**, 3573–3587.e3529 (2021).
61. McGinnis, C. S., Murrow, L. M. & Gartner, Z. J. DoubletFinder: doublet detection in single-cell RNA sequencing data using artificial nearest neighbors. *Cell Syst.* **8**, 329–337.e324 (2019).
62. Korsunsky, I. et al. Fast, sensitive and accurate integration of single-cell data with Harmony. *Nat. Methods* **16**, 1289–1296 (2019).
63. Zhu, A., Ibrahim, J. G. & Love, M. I. Heavy-tailed prior distributions for sequence count data: removing the noise and preserving large differences. *Bioinformatics* **35**, 2084–2092 (2018).
64. Wu, T. et al. clusterProfiler 4.0: A universal enrichment tool for interpreting omics data. *Innovation* **2**, 100141 (2021).
65. Yang, X. et al. SPP1 promotes the polarization of M2 macrophages through the Jak2/Stat3 signaling pathway and accelerates the progression of idiopathic pulmonary fibrosis. *Int. J. Mol. Med.* **54**, 89 (2024).
66. Pasupuleti, B. G., Khongsti, K., Das, B. & Bez, G. 1,2,3-Triazole tethered 1,2,4-trioxanes: Studies on their synthesis and effect on osteopontin expression in MDA-MB-435 breast cancer cells. *Eur. J. Med Chem.* **186**, 111908 (2020).

Acknowledgements

We kindly acknowledge the contributions of the personnel of the animal facilities and the Center for Omics Sciences (COSR) at the IRCCS Ospedale San Raffaele for technical support. The work was supported by the European Union's Horizon 2020 research and innovation program under the Marie Skłodowska-Curie grant agreement No 860034 to SB and FTF; Italian Ministry of Education-University-Research (2022TR9N4R to SB); Fondazione Cariplo "Biomedical Research conducted by young researchers" (2018-0102 to EA); Cariplo Telethon Alliance (GJC22013 to EA); Italian Ministry of Education-University-Research (2022TT8Z3M and P20223HEZC to EA); CB was supported by Fondazione Umberto Veronesi.

Author contributions

FTF: Conceptualization, Formal analysis, Investigation, Methodology, Project administration; Software, Visualization, Writing – original draft; MB: Investigation, Formal analysis, Visualization; RG: Investigation; CB: Investigation; CDO: Investigation; AST: Software; VB: Investigation, Formal Analysis; RM: Resources; AF: Resources, Methodology EA: Resources, Funding acquisition; Methodology; Writing – review & editing; SB: Conceptualization; Funding acquisition; Project administration; Resources; Supervision; Writing – review & editing.

Competing interests

The authors declare no competing interests.

Additional information

Supplementary information The online version contains supplementary material available at https://doi.org/10.1038/s42003-026-10194-z.

Correspondence and requests for materials should be addressed to Silvia Brunelli.

Peer review information *Communications Biology* thanks Gaoxian Chen and the other anonymous reviewer(s) for their contribution to the peer review of this work. Primary Handling Editors: Ngan Huang and Mengtan Xing.